

**Mechanical and Cellular Response to Biomineralization of Ovalbumin Scaffolds for
Bone Tissue Engineering**

Kevin T. Sheets

Thesis submitted to the faculty of the Virginia Polytechnic Institute and State University
in partial fulfillment of the requirements for the degree of

Master of Science
In
Materials Science and Engineering

Abby W. Morgan, Chair
Judy S. Riffle
Sean G. Corcoran

May 3, 2010
Blacksburg, Virginia

Keywords: ovalbumin, calcium phosphate, tissue engineering, simulated body fluid

Copyright 2010

Mechanical and Cellular Response to Biomineralization of Ovalbumin Scaffolds for Bone Tissue Engineering

Kevin T. Sheets

ABSTRACT

Studies regarding the feasibility of ovalbumin (OVA) as a bone scaffold material have found its cost, availability, interaction with cells, and ability to degrade in the body into safe byproducts to be ideal for such an application. However, weak mechanical properties cause hesitation in the use of OVA as a scaffolding material in much stronger native tissue. To enhance the mechanical strength of the OVA scaffolds without compromising *in vitro* cellular performance, Ca-P crystals were grown on unmodified OVA and phosphonated OVA (p-OVA) samples via biomineralization processes using 5x-concentrated simulated body fluid (5x SBF).

Electron microscopy (ESEM/EDS) data confirm the formation of Ca-P crystals on the surface of OVA and p-OVA scaffolds. Mechanically, rheology data measured a minimum of a three-fold increase in each mineralized scaffold's complex shear modulus over unmineralized counterparts. Degradation in a PBS+collagenase XI environment showed that mineralization extended total time to degradation. It was also shown that the formation of the Ca-P crystals had no negative effects on *in vitro* cell studies. To measure cellular response, a live/dead assay was conducted to confirm cell viability after 24 hours.

In conclusion, improvements were made to mechanical strength without compromising *in vitro* cell-scaffold response. While it remains unknown whether the increase in strength is adequate for use as a bone scaffold, future work should focus on gathering necessary information to study OVA scaffolds in animal models for eventual consideration as a bone graft substitute material.

Acknowledgements

I would like to express my gratitude and appreciation for those who made this project possible. First, I owe many thanks to the Macromolecules and Interfaces Institute (MII) and the Materials Science and Engineering (MSE) Departments at Virginia Tech for their funding and support. I also want to thank my Advisor, Dr. Abby Morgan, for her constant guidance, direction, and encouragement, and for welcoming me into her group. I am grateful for my committee members, Dr. Judy Riffle and Dr. Sean Corcoran, for their collaboration and advice. Thanks to the Institute for Critical Technology and Applied Science (ICTAS) for their facilities and equipment which made the research possible. Special thanks to David Berry and Steve McCartney for their training and aid with lab equipment that took wonderful pictures and gathered important data. Much of this research would not be possible without the collaboration from specific members of Dr. Riffle's group: Dr. Yinnian Lin, Suzanne Hamm, Nipon Pothayee and Nikorn Pothayee. Lastly, I want to express my utmost appreciation for the constant help and encouragement from everyone in Dr. Morgan's lab group: Tyler Horseman, Satyavrata Samavedi, Ben Glasemann, and Adwoa Baah-Dwomoh. I wish you the best in your future endeavors.

Table of Contents

Chapter 1: Introduction	1
Chapter 2: Materials and Methods	9
2.1 Scaffold Design and Fabrication	9
2.1.1 OVA Solution	9
2.1.2 p-OVA Solutions	9
2.1.3 Scaffold Fabrication	10
2.2 Biomineralization	11
2.2.1 Simulated Body Fluid (SBF)	11
2.2.2 SBF Treatment	13
2.2.3 Ca-P Crystal Growth Profile	13
2.3 Scaffold Characterization	14
2.3.1 ESEM/EDS	14
2.3.2 Mechanical Testing	15
2.3.3 Degradation	15
2.4 <i>In Vitro</i> Cell Studies	16
2.4.1 Cell Culture	16
2.4.2 Live/Dead Assay	17
2.4.3 Cytotoxicity – MTT Assay	17
Chapter 3: Results	19
3.1 Scaffold Design and Fabrication	19
3.2 Biomineralization	21
3.2.1 SBF Treatment	21
3.2.2 Crystal Growth Profile	23
3.3 Scaffold Characterization	26
3.3.1 EDS	26
3.3.2 Mechanical Testing	33
3.3.3 Degradation	34
3.4 <i>In Vitro</i> Cell Studies	35
3.4.1 Live/Dead Assay	35
3.4.2 Cell Proliferation – MTT Assay	37

Chapter 4: Discussion	38
4.1 Scaffold Design and Fabrication	38
4.2 Biomineralization	38
4.2.1 SBF Treatment.....	38
4.2.2 Crystal Growth Profile.....	41
4.3 Scaffold Characterization.....	43
4.3.1 Mechanical Testing – Rheology	43
4.3.2 Mechanical Testing – Degradation Study	44
4.4 <i>In Vitro</i> Cell Studies.....	45
4.4.1 Live/Dead Assay.....	45
4.4.2 Cytotoxicity – MTT Assay	45
Chapter 5: Conclusions	47
5.1 Future Work	48
Chapter 6: References	50
Appendix A: Bisphosphonation of Hydroxyethyl Chitosan (HEC)	54
A.1 Introduction.....	54
A.2 Materials and Methods	54
A.3 Results and Discussion	55
Appendix B: Biomineralization of Bacterial Cellulose.....	57
B.1 Introduction.....	57
B.2 Materials and Methods.....	57
B.3 Results and Discussion	58

List of Figures

Figure 1: Lysine modifications for each of the p-OVA scaffold types, including (A) deprotonated VPA, (B) protonated VPA, (C) DME, and (D) BIS	7
Figure 2: Each well of the 12-well plate produced 4 scaffolds after being cut and removed with cork borer	19
Figure 3: The porosity of ovalbumin scaffolds. (A) Pores cover the entire surface of the material, (B) interconnecting pores can be seen (C) Mineralization seen through a pore on VPA scaffold, (D) Ca-P crystal shown growing inside a pore, with more pores visible in the background.....	20
Figure 4: The porosity of ovalbumin scaffolds. (A) Pores cover the entire surface of the material, (B) interconnecting pores can be seen	21
Figure 5: OVA scaffolds after 2 hr immersion in 1x SBF yielded no mineralization	21
Figure 6: Large-scale Ca-P crystallization on (A) OVA, (B) DME, (C) VPA, and (D) VPA in a pore wall.....	22
Figure 7: (A) OVA 2 hr after 1x SBF treatment. No Ca-P crystallization seen, (B) p-OVA fracture surface 6 hr after 5x SBF treatment. A thin layer of Ca-P crystals is seen on the surface.	23
Figure 8: Scaffold mass increase as a function of SBF treatment time	24
Figure 9: Ca-P crystallization upon completion of crystal growth profile study of (A) unmineralized OVA, (B) mineralized OVA, (C) mineralized DME, and (D) mineralized BIS 20 scaffolds. Total incubation time was 15 days in 5x SBF. Magnifications vary.....	25
Figure 10: EDS on large-scale crystal after 72 hr incubation in 5x SBF. (A) ESEM image of the spot size scanned, (B) EDS elemental composition of the spot.....	26
Figure 11: EDS data for unmineralized OVA. (A) ESEM image of scanned spot, (B) Color map locating primarily Na and Cl, (C) Elemental composition of with dominant peaks highlighted	28
Figure 12: EDS data for mineralized OVA. (A) ESEM image of scanned spot, (B) Color map locating Ca and P, (C) Elemental composition of with dominant peaks highlighted	29
Figure 13: EDS data for DME. (A) ESEM image of scanned spot, (B) Color map locating Ca and P, (C) Elemental composition of crystals with dominant peaks highlighted	30
Figure 14: EDS data for mineralized BIS 10. (A) ESEM image of scanned spot, (B) Color map locating Ca and P, (C) Elemental composition of with dominant peaks highlighted	31
Figure 15: EDS data for BIS 20. (A) ESEM image of scanned spot, (B) Color map locating Ca and P, (C) Elemental composition of with dominant peaks highlighted	32
Figure 16: Rheology data shows mineralized samples have stronger complex shear modulii than unmineralized counterparts	33
Figure 17: Degradation in PBS+Collagenase XI shows mineralization prolongs time to complete degradation.....	34
Figure 18: Combined live/dead images of (A) Unmineralized OVA, (B) Mineralized OVA, (C) Unmineralized DME, (D) Mineralized DME, (E) Unmineralized BIS 10, and (F) Mineralized BIS 10 scaffolds	36
Figure 19: Variation in MTT assay results in inconclusive data for (A) 1-day incubation and (B) 3-day incubation times	37
Figure 20: (A) OVA 2 hr after 1x SBF treatment. No Ca-P crystallization seen, (B) OVA surface showing water damage	39

Figure 21: Schematic illustrating mineralization of a VPA scaffold.....	40
Figure 22: (A) Live stain on unmineralized BIS 10. All cells are viable, as indicated by green stain. Image (B) shows scaffold autofluorescence causes these same cells to be visible with the dead stain despite being viable.	45
Figure 23: Modification of amine-containing HEC with bisphosphonates via an aza-Michael reaction [60].....	55
Figure 24: Optical microscopy of HEC (A) and OVA (B) sponges at 100x	56
Figure 25: MTT Assay on HEC scaffolds	56
Figure 26: Schematic of a bioreactor/pump system for creation of mineralized BC tubes [61].	58
Figure 27: FESEM images taken at the same magnification: (A) pure tube out BC scaffold, (B) mineralized tube out BC scaffold, (C) pure pellicle BC scaffold, (D) mineralized pellicle BC scaffold, (E) pure tube in BC scaffold, (F) mineralized tube in BC scaffold [61].....	60
Figure 28: XRD spectra of (a) pure BC and (b) mineralized BC with the asterisks indicating the primary peaks used to identify the calcium phosphate crystal [61].....	61
Figure 29: Fluorescent microscopy images (blue stain = nucleus, red stain = actin): (A) pure BC control scaffold and (B) mineralized BC scaffold [61].	62
Figure 30: ALP activity for BC substrates [61]	63

List of Tables

Table 1: Nomenclature of ovalbumin and its modifications.....	10
Table 2: Salt concentrations found in SBF [36].....	12
Table 3: Amounts of salts used to create both 1x and 5x SBF	12
Table 4: Elemental composition of large crystal on p-OVA after 72 hr in 5x SBF	27
Table 5: Elemental composition of scanned spot for unmineralized OVA	28
Table 6: Elemental composition of scanned spot for mineralized OVA	29
Table 7: Elemental composition of scanned spot for mineralized DME	30
Table 8: Elemental composition of scanned spot for mineralized BIS 10.....	31
Table 9: Elemental composition of scanned spot for mineralized BIS 20.....	32
Table 10: Average XPS data for each treatment and substrate [61]	59
Table 11: EDS spectrum data of elements present on crystal observed and off of the crystal observed [61].	61

List of Equations

(1).....	15
(2).....	15

List of Abbreviations

ALP	Alkaline Phosphatase
BC	Bacterial Cellulose
BIS	Bisphosphonate
BMP	Bone Morphogenic Protein
cdHAp	Calcium-deficient Hydroxyapatite
CDU	Collagenase Digestive Unit
DBM	Demineralized Bone Matrix
DI	Deionized
DME	Dimethyl Ester
DMEA	Dimethyl Ethyl Acrylate
DMVP	Dimethyl Vinyl Phosphonate
DTT	Dithiothreitol
ESEM	Environmental Scanning Electron Microscope
FBS	Fetal Bovine Serum
FESEM	Field-Emission Scanning Electron Microscope
g	Gram
GA	Glutaraldehyde
HEC	Hydroxyethyl Chitosan
Hz	Hertz
hr	Hour
μL	Microliter
M	Molar
MEM	Minimum Essential Media
mg	Milligram
mm	Millimeter
mL	Milliliter
mM	Millimolar
N	Normal
OVA	Ovalbumin
PBS	Phosphate Buffered Saline
PEG	Polyethylene Glycol
PCL	Polycaprolactone
PLGA	Poly(lactic-co-glycolic acid)
pOVA	Phosphorylated Ovalbumin
PVC	Poly Vinyl Chloride
SEM	Scanning Electron Microscope
VPA	Vinyl Phosphonic Acid
XPS	X-Ray Photoelectron Spectroscopy
XRD	X-Ray Diffraction

Chapter 1: Introduction

Bone Fracture and Healing

When natural bone suffers a fracture, a physiological healing response is initiated and, with adequate immobilization and assuming no complications arise, full healing is typically experienced [1, 2]. Bone function is restored and, except in the case of non-union or severe deformity, minimal long-term damage occurs. However, if trauma to the bone causes significant tissue loss or when the separation created by a fracture reaches or exceeds a critical size, the body's physiological response alone is no longer able to restore healing to the injury site. In these cases, the separation between healthy cells is too great for the deposition of new bone required for healing to occur and function is permanently lost [3, 4]. To restore bone integrity and function and initiate full healing in a critical-size defect, a filler material must be placed in the gap between the segments of healthy bone to guide cell growth [5]. The filler material used to fuse broken segments of bone is known as a bone graft.

Inadequacies of Current Grafting Technologies

An injured patient currently has three options for bone graft materials: those taken from the injured patient (autografts), those taken from a donor (allografts), or those designed and fabricated from outside materials (scaffolds).

Autografts are typically taken from the patient's iliac crest or the hip bone, although they can also be removed from the femur, tibia, or ribs [6, 7]. Since the procedure is invasive – requiring healthy segments of healthy bone to be cut and removed – donor site morbidity is cited as a primary concern for both patients and doctors [8, 9]. It is often reported that the harvesting procedure is more painful than the grafting procedure itself [10, 11]. The methods and tools used

while harvesting bone are still being modified to reduce the pain associated with autografts, but an ideal solution is to avoid a second incision altogether [12-14].

An allograft is a bone-like material that comes from donors, usually in the form of cadaverous demineralized bone matrix (DBM). Since using an allograft involves the implantation of foreign material into the patient's body, DBM must be cleansed of all cellular traces to prevent possible disease transmission [15, 16]. Bacterial infection, HIV transmission, and identification of bacterial and viral contamination in tissue have all been associated with bone allografts that did not undergo terminal sterilization [17]. Sterilization and decalcification processes weaken DBM, resulting in putty-like material that can be packed into a wound site. Marshall Urist first reported the use of cadaverous bone from a human donor as an osteoinductive material in a 1965 animal study [18]. In this paper, Urist devitalized and decalcified the bone in a sterile solution of 0.6 N HCl, then implanted the material in animal wound sites. After implanting the DBM, Urist found that cells associated with the inflammatory and healing responses were drawn to the affected area due to the degradation products derived during decalcification, later identified as bone morphogenic proteins (BMP) [19]. The majority of implants resulted in osteoinduction, supposedly a result of BMP presence. While relatively effective as a bone graft material, there is a wide variation in the quality of the DBM from donor to donor. Often, the surgeon does not know any specific characteristics of the DBM used during implantation [15]. The potential complications of donor and cadaver bone graft sources could be avoided if a safe and effective bone graft substitute material could be developed.

A Materials Solution

Every year, over two million bone grafting procedures are performed across the world [20, 21]. It is estimated that 90% of these grafts are either autografts or allografts [22]. Despite risks to the patient, autografts and allografts remain preferable to engineered solutions [23, 24]. While progress towards an engineered solution has been made in recent years, the ideal scaffold has not yet been developed. The design and fabrication of three-dimensional bone scaffolds is a primary focus in tissue engineering due to the medical and financial benefits they theoretically provide [25-28]. There are several materials that possess the structure and properties required to initiate bone regeneration, yet lack a proper response in the body such as degrading into safe byproducts over an acceptable timeframe. On the other hand, several materials interact quite favorably in the body, yet do not have the strength or porosity to promote bone healing.

There is debate over which materials class provides the most promise for bone tissue engineering [28, 29]. Metals, ceramics, and polymers all have advantages and disadvantages as scaffold material candidates. While metals and ceramics inherently possess mechanical strength comparable to natural bone, implants are not typically biodegradable. Ideally, the scaffold would promote self-healing, degrading into safe byproducts as native tissue permeates the material construct.

Ovalbumin (OVA), a natural polymer found in avian egg whites, is one such material. Its low cost, high availability, favorable interaction with native tissue, and ability to degrade in the body into safe byproducts make it an interesting bone scaffold material candidate [30]. However, past studies have shown OVA to perform weakly under mechanical testing when compared to natural bone strength. Theoretically, the mismatch of mechanical strength will produce stress concentrations at the scaffold-bone interface and lead to premature failure. A

similar phenomenon is seen *in vivo* with titanium hip implants [31]. Ovalbumin scaffolds are simply too weak to be used in load-bearing applications.

Natural bone's inherent combination of strength and flexibility is attributed to its composite structure. In natural tissue, collagen fibrils arrange into a triple-helix structure and form a porous network on which hydroxyapatite (HAp) crystals are found. The collagen fibrils (~30 wt% of dry bone) provide flexibility, while the HAp (~70 wt% of dry bone) provides stiffness [32, 33]. Individually, the collagen fibrils are too compliant to support the loads required during bone function, and the hydroxyapatite is too brittle. But together, the composite material allows bone to be both flexible and strong. The idea is therefore to mimic this structure and create an ovalbumin/HAp composite, which relies on the ovalbumin phase for elasticity and on HAp for strength. Such a material would be stronger and perform more favorably in the body due to the presence of crystals that are normally seen *in situ*.

Biom mineralization

A common method used to grow bone-like mineral is the process of biom mineralization. In the late 1980's and early 1990's, Kokubo discovered that a glass ceramic containing apatite and wollastonite formed a thin layer of apatite when immersed in a simulated body fluid (SBF) [34]. This fluid contained salt ion concentrations found in human blood plasma, slightly modified to favor apatite growth. Kokubo then tested other materials in SBF including SUS316 stainless steel, platinum metal, polyethylene, and polymethylmethacrylate. It was found that all substrates would form an apatite layer within one week provided they were placed near a glass dissolving the calcium and silicate ions in SBF.

After this biom mineralization process had been studied by several groups, it became apparent that the kinetics of the apatite formation could be controlled based on the ion

concentrations found in the SBF [35, 36]. Barrere found that a solution of SBF containing 5x the ion concentrations in human blood plasma would form a uniform layer of Ca-P crystals on Ti6Al4V within 24 hr [35]. Jayasuriya noted bone like mineral on three-dimensional porous poly(lactic –co glycolic acid) (PLGA) scaffolds in just 36-48 h, as opposed to the 1-2 week period required by 1x SBF [36].

The formation of Ca-P crystals has been shown to mechanically strengthen various polymer scaffolds, including those made from chitosan, chitosan-alginate hybrids, poly(lactic-co-glycolic acid) (PLGA), polycaprolactone (PCL), and others [37-42]. This process will therefore be used to enhance the mechanical strength of OVA scaffolds.

While SBF has definitively been shown to cause growth of Ca-P minerals on various surfaces, its validity as a predictor of *in vivo* bioactivity is a source of debate in bioengineering literature [43, 44]. Proponents argue SBF models salt concentrations found in human blood plasma to an extent that it can predict *in vivo* bone binding, but dissenters find fault with the absence of control on other physiological conditions such as carbon dioxide levels. In either case, apatite formation has been shown to improve osteoconductivity, meaning mechanical strength can be enhanced without negatively affecting cell-scaffold interactions [45].

Phosphorylation of Ovalbumin

Many bone scaffold materials inherently possess the ability to nucleate and grow calcium phosphate crystals when immersed in SBF. It remains unclear precisely what material properties promote or inhibit the formation of this layer of crystals, but without surface modification, OVA scaffolds did not produce mineralization within one week when 1x SBF was used. However, studies have identified scaffold surface charge as an important parameter. Therefore, OVA was

phosphonated (p-OVA) to enhance the material's ability to nucleate and grow crystals. The newly added phosphonates serve as nucleation sites for Ca-P crystallization.

Phosphonates are added by Michael addition to the free amines on lysine groups in the OVA amino acid sequence. Farrar determined that ovalbumin scaffolds could be crosslinked with varying amounts of glutaraldehyde (GA) [30]. However, the amounts used were all in excess of what the reaction required. It could not be determined based on that study whether OVA scaffolds required all 19 lysine groups per chain to be used during crosslinking reaction with GA. In this study, it was shown that OVA could be crosslinked without using all 19 lysine groups per chain. Those not used in the GA crosslinking reaction were used for phosphorylation – adding phosphonate groups onto the free amine group.

To vary surface charge and pH sensitivity, different types of phosphonates were added. Figure 1 below outlines the four different lysine group modifications used throughout this study. The four total scaffold types consist of unmodified ovalbumin (OVA) and three phosphonated (p-OVA) substrates: vinyl phosphonic acid (VPA), dimethyl ester (DME), and bisphosphonate (BIS). Each of these phosphonates was added via Michael addition. Phosphonates function as nucleation sites for Ca-P crystal nucleation and growth.

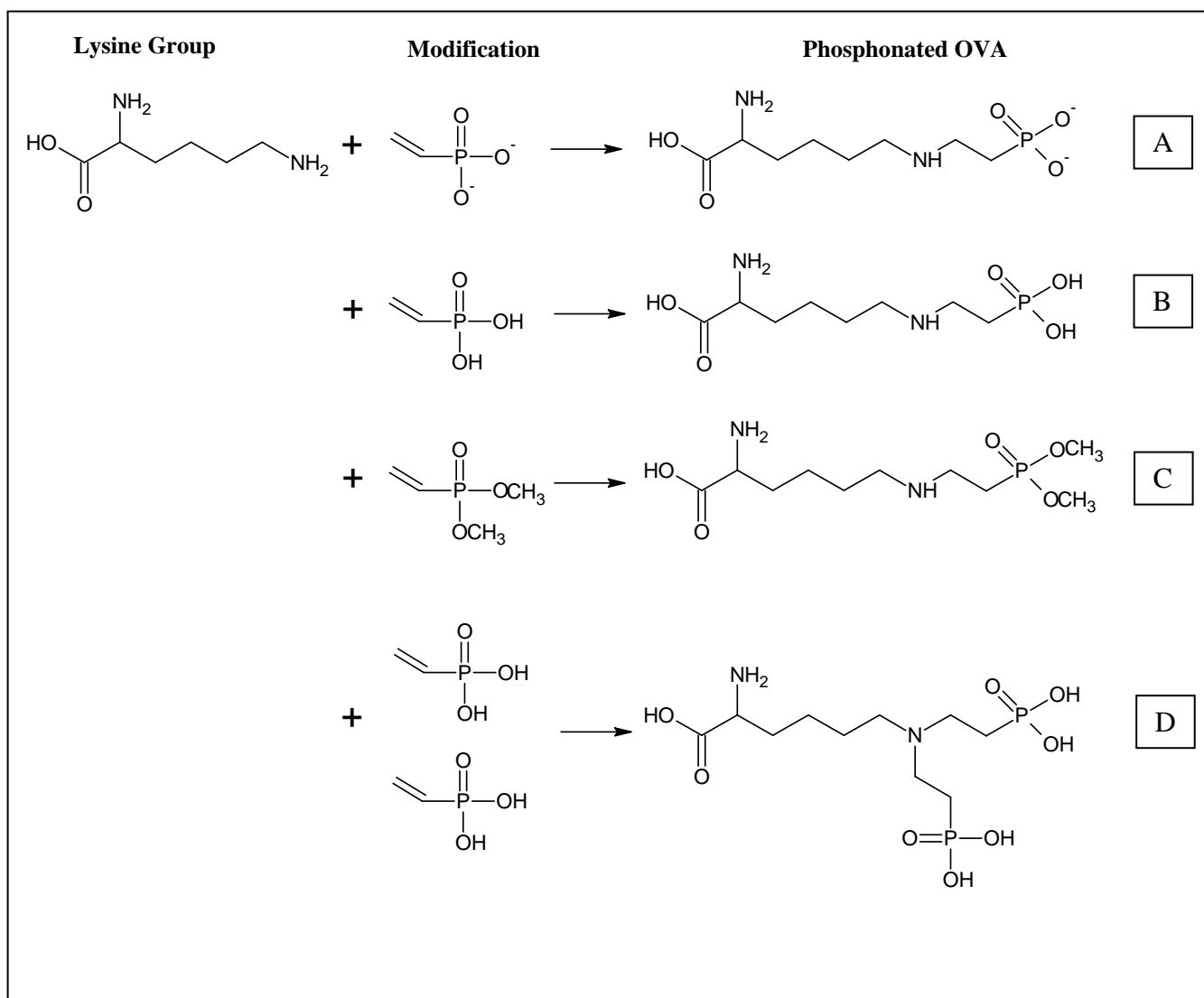


Figure 1: Lysine modifications for each of the p-OVA scaffold types, including (A) deprotonated VPA, (B) protonated VPA, (C) DME, and (D) BIS

Cell Studies

Past studies showed OVA scaffolds provide an environment conducive to mouse preosteoblast adhesion [30]. Cellular response to surface modifications must be measured to ensure any changes to cytotoxicity levels are negligible. To measure this response, MC3T3-E1 mouse preosteoblastic cells can be used to model osteoblast response to a foreign material *in*

vitro. As such, this cell line is extensively used in bone-related physiological studies [46-48]. This cell line was therefore used in live/dead staining and MTT cytotoxicity measurements in this study.

Chapter 2: Materials and Methods

2.1 Scaffold Design and Fabrication

Three-dimensional porous scaffolds were designed to mimic natural bone's structure. Mimicking the natural environment of preosteoblasts optimizes their ability to behave as they would *in vivo*, maximizing migration and ultimately allowing growth throughout the material. Scaffolds were made from both the normal OVA solution as well as three phosphonated ovalbumin solutions (p-OVA): VPA, DME, and BIS.

2.1.1 OVA Solution

To create the ovalbumin solution, 5g albumin (from chicken, Sigma) was dissolved in 50 mL DI water using a shaker. Then 30 mL borate buffer was added along with 0.01 g dithiothreitol (DTT). The solution was shaken until homogenous, and then underwent dialysis to a neutral pH using snakeskin tubing for three days. The solution was then stored in the refrigerator until use.

2.1.2 p-OVA Solutions

Four different p-OVA solutions were created to enhance the amount of Ca-P mineralization due to SBF treatments. Table 1 below provides an overview of the various phosphonated solutions as well as the nomenclature used throughout this study.

Table 1: Nomenclature of ovalbumin and its modifications

Class	Class Abbreviation	Modification to Lysine	Modification Amount	Material Abbreviation
Unmodified Ovalbumin	OVA	None	None	OVA
Phosphonated Ovalbumin	p-OVA	Vinyl phosphonic acid	10%	VPA
		Dimethyl Ester	10%	DME
		Bisphosphonate	10%	BIS 10
		Bisphosphonate	20%	BIS 20

To make VPA solution, 20 mL OVA solution was added to a 100 mL round-bottom flask. Then 67 mg dimethyl vinyl phosphonate (DMVP) and 2 mL deuterium monoxide (D₂O) was added to the solution. After adjusting the pH, the solution was stirred at RT for 24 hrs. DME was made in similar fashion.

BIS solution was created by adding 20 mL OVA solution to a 100 mL round-bottom flask, then adding 67 mg diphosphonate ethyl acrylate (DPEA) and 2 mL D₂O. After adjusting the pH to 7, the solution was stirred at RT for 24 hrs.

2.1.3 Scaffold Fabrication

To make the three-dimensional porous OVA and p-OVA scaffolds, 1g NaCl from 150 – 212 μm diameter was added to each well of a 12-well plate as a porogen. Next, 2.5 mL OVA or p-OVA solution was added to each well. To crosslink the solution, 25 μL 10% (v/v) GA was added to each well, and then the contents of each well were stirred together with a pipette tip. The well plate was left on a platform shaker at 120 rpm for 18-24 hours. Upon completion of the crosslinking reaction, the scaffolds were punched out of their well plates using a cork borer. The scaffolds were then placed in a 250 mL beaker and washed in 200 mL glycine (0.1 M) by stirring

at 37 °C for one hour. After this time, the scaffolds were rinsed in 200 mL DI water at 37 °C for three days, replacing the water twice daily. Finally, the scaffolds were frozen overnight in a -80 °C freezer and then freeze dried.

2.2 Biomineralization

The process of taking a material sample, immersing it in SBF, and incubating it under physiological temperature (37 °C) to nucleate and grow bone-like apatite mineral on the material surface is known as biomineralization.

2.2.1 Simulated Body Fluid (SBF)

SBF is a solution containing the salt ion concentrations found in human blood plasma. Both 1x and 5x the normal physiological amounts were eventually used. In this study, the 1x SBF was prepared by dissolving various salts into DI water as first reported by Kokubo [34] while the 5x SBF was prepared using the method reported by Jayasuryia, who demonstrated that 5x SBF sped up the formation of a bone-like apatite layer without changing the type of apatite that formed on the material surfaces [36]. The 5x SBF was used to reduce incubation times. Table 2 below provides the salt ions used along with their concentrations in both 1x and 5x SBF solutions.

Table 2: Salt concentrations found in SBF [36]

Ions	Blood Plasma	1x SBF	5x SBF
Na ⁺	142.0	145.2	726.0
K ⁺	5.0	5.0	25.0
Mg ⁺	1.5	1.5	7.5
Ca ²⁺	2.5	2.5	12.5
Cl ⁻	103.0	152.0	760.0
HCO ₃ ⁻	27.0	4.2	21.0
H ₂ PO ₄ ⁻	1.0	1.0	5.0
SO ₄ ²⁻	0.5	0.5	2.5
pH	7.2-7.4	7.4	6.8

To achieve these salt ion concentrations, seven chemicals were used. The amount and order of each used to create the 1x and 5x SBF formulas are shown below.

Table 3: Amounts of salts used to create both 1x and 5x SBF

Salt	1x SBF (g)	5x SBF (g)
1. NaCl	6.55	40.62
2. KCl	0.37	1.86
3. CaCl ₂ -2H ₂ O	0.37	1.84
4. MgCl ₂ -6H ₂ O	0.31	1.52
5. NaH ₂ PO ₄	*0.18	0.60
6. Na ₂ SO ₄	0.07	0.36
7. NaHCO ₃	2.27	1.76
8. Tris(hydroxymethyl)aminomethane	6.06	-

* sodium phosphate, dibasic dehydrate used instead (Na₂HPO₄-2H₂O)

Preparation varied between the 1x SBF and the 5x SBF since the 5x SBF solution contains a large amount of salt ions that have a tendency to precipitate out of solution. To avoid accidental precipitation in the 5x solution, bicarbonate solution was made separate from the stock solution. These two solutions were then combined and immediately used.

2.2.2 SBF Treatment

As a pilot study, OVA scaffolds were immersed in 1x SBF for various periods of time to determine the growth pattern of Ca-P crystals. Two OVA scaffolds were placed in each well of a 6-well plate. Then, 10 mL of 1x SBF was added to each well. The plate was covered in parafilm to prevent complete evaporation and placed in a 37 °C oven. Samples were removed after 2 hr, 4 hr, 24 hr, 72 hr, and 168 hr. Samples incubated for longer than 24 hr had SBF changed every 24 hr. Once removed, the samples were rinsed under a stream of DI water to wash off any soluble salts, frozen for 24 hr, and freeze-dried for 48 hr. They were then examined by ESEM to characterize any crystallization present.

After realizing that the 1x SBF treatments did not produce crystallization within one week, it was decided that 5x SBF could be used to increase reaction kinetics. During this treatment phase, the scaffolds were placed in 6-well plates as before. Stock and bicarbonate solutions were mixed together to form the 5x SBF, which was immediately added to each well, 10mL per well. The plate was then covered in parafilm and placed in a 37 °C oven for 72 hr, exchanging SBF every 24 hr. Upon completion of the SBF treatment schedule, each sample was taken out of its well, rinsed under a stream of DI water, and freeze-dried. Doing so removed excess ions that had precipitated onto the OVA surface and were not chemically bonded.

2.2.3 Ca-P Crystal Growth Profile

Since it was found that immersion in 5x SBF resulted in Ca-P mineralization, an experiment was conducted to determine temporal dependence on the crystal growth profile of OVA and p-OVA substrates. To measure this, OVA and p-OVA scaffolds were created. Six scaffolds of each type were immersed in 5x SBF (60 mL: 48 mL stock solution, 12 mL

bicarbonate) and placed in a 37 °C incubator. After various amounts of time, which ranged from 24 hr during the first week of treatment to 72 hr during the second week, the scaffolds were removed from the incubator and 5x SBF solution, dried on a kimwipe, and weighed. After weighing, the samples were immersed in fresh 5x SBF and placed back in the oven. The weight change for the scaffold types was tracked to determine how much weight the scaffolds gained. This study continued until scaffolds no longer increased in mass, a process that took over two weeks.

2.3 Scaffold Characterization

2.3.1 ESEM/EDS

Images of the OVA and p-OVA scaffold types help characterize differences between the surface types, including pore size and relative amount of mineralization seen. FEI's Quanta 600 FEG Environmental Scanning Electron Microscope (ESEM) with Energy Dispersive Spectroscopy (EDS) was used to both take images and measure atomic composition of the scaffolds' surfaces. Since the scaffolds are electrical insulators, a thin layer (15-20 nm) of metallic gold-palladium was sputter-coated onto each scaffold to provide additional electrons for the instrument to measure. Images were taken at 100x, 500x, and 2,000x magnifications using a 5 kV source beam at a working distance approximately 8 mm. The Energy Dispersive Spectroscopy (EDS) used in this experimentation was a feature included with the FEI Quanta 600 FEG ESEM.

2.3.2 Mechanical Testing

To measure changes in mechanical stiffness, rheological studies were performed on the scaffolds using TA Instruments' AR-G2 rheometer. Samples were tested between parallel plates 8 mm in diameter. They were held at 10 Pa pressure while a frequency sweep was conducted from 0.1 Hz to 10 Hz.

Data resulting from the rheology measurements return two values: storage modulus (G') and loss modulus (G''). The storage modulus is a real number that measures elastic response, while the loss modulus is an imaginary number that measures viscous response. Together, these values can be used to determine a complex shear modulus value (G^*). The complex shear modulus combines the elastic and viscous responses to provide a single value that characterizes total shear response [49, 50].

$$G^* = G' + iG'' \text{ where } i = \sqrt{-1} \quad (1)$$

$$|G^*| = \sqrt{(G')^2 + (G'')^2} \quad (2)$$

The G^* values of OVA and p-OVA scaffolds will then be compared to determine whether Ca-P mineralization increases mechanical stiffness.

2.3.3 Degradation

Biodegradability is another important parameter for bone scaffold materials. Ideally, the scaffold would degrade at the same rate that bone rebuilds. The degradation rates of the scaffolds were measured to determine whether the Ca-P crystallization altered degradation patterns. While many *in vitro* degradation environments simulate *in vivo* temporal conditions, previous studies have shown that soaking the samples in PBS and collagenase type I provided an

accurate estimate of *in vivo* performance. Since previous work has established the *in vitro* degradation time for OVA scaffolds as five weeks and it was estimated that mineralization would slow this process, a more rigorous environment was desired to speed degradation [30]. Collagenase XI was chosen since it has the highest collagenase activity, measured in collagenase digestive units (CDU) per mg solid.

Therefore, both OVA and p-OVA scaffolds were immersed in PBS and collagenase type XI during the degradation study. Three samples of each scaffold type as well as an unmineralized control were placed individually in micro-centrifuge tubes. For each scaffold, 1 mL PBS and 1 mg collagenase were added to the tubes, which were stored together in a holding bracket. The bracket was then placed in a 37 °C water bath for two days. After that time period, the scaffolds were removed from their tubes, weighed, and then put back their tubes along with a fresh dose of PBS and collagenase.

2.4 *In Vitro* Cell Studies

2.4.1 Cell Culture

To determine the effect crystallization had on cell response, two different *in vitro* cell studies were carried out. In each of these studies, MC3T3-E1 (clone 26) murine pre-osteoblast cells (ATCC) were seeded onto each of the scaffold types to determine whether they preferred adhering to crystallized or uncrystallized scaffolds.

Cells were cultured in α -Minimum Essential Media (α -MEM) with 10% v/v Fetal Bovine Serum (FBS) and 1% v/v Antibiotic/Antimycotic. Media was changed every 72 hr. Cells were split when 80% confluency was reached. Cells were used between passages 8 and 10. Aseptic technique was used throughout.

2.4.2 *Live/Dead Assay*

The live/dead assay (Sigma) provides a simultaneous determination of viable and dead cells. In this study, MC3T3-E1 preosteoblasts were seeded onto the OVA and p-OVA scaffolds and incubated for 24 hr. After that time period, cells were stained with both Calcein-AM and Propidium iodide stains. Calcein-AM stains viable cells only, which emit green fluorescence when excited. Propidium iodide permeates the membrane of dead cells, causing them to fluoresce red when excited. The ratio of cells stained green to red is measured to quantify cell viability. If cells are viable, the rest of the cell studies may be performed. If the test returns negative and all the cells have died, there is no need to perform the other tests as the cells are unable to live on the scaffold surfaces.

Fluka's Live/Dead Cell Double Staining Kit (Sigma) contained two solutions which were used to create the fluorescent stain. To make the stain, 5 μ L Solution A (live stain) and 2.5 μ L Solution B (dead stain) were added to 2.5 mL PBS. After aspirating media, each well was washed twice in 1 mL PBS. Cells were then stained by adding 100 μ L stain to each well and activated by 15-minute incubation.

2.4.3 *Cytotoxicity – MTT Assay*

Cytotoxicity studies are used to determine the amount of toxic effect a substrate has on cells. In the MTT assay, cells are seeded onto triplicates of each scaffold type and incubated for two different periods of time. Both 3-day and 1-day measurements are made to evaluate the change in toxicity over time. In this assay, the viable cells convert MTT to a water-insoluble formazan crystal, which changes color when dissolved with acidic isopropanol. The purple-to-yellow color change is measured spectrophotometrically at 570 nm in a microplate reader. Cells

were seeded 50,000 cells/well to ensure adequate absorbance readings at 570 nm. Data was normalized to a control triplicate which also contained 50,000 cells each.

Chapter 3: Results

3.1 Scaffold Design and Fabrication

Three-dimensional porous scaffolds were created for both OVA and p-OVA substrates. After cutting samples out of the 12-well plate, scaffolds were cylindrical, approximately 8 mm in diameter and 4 mm thick. Samples slightly lost cylindrical shape after freezing and freeze-drying (Figure 2).

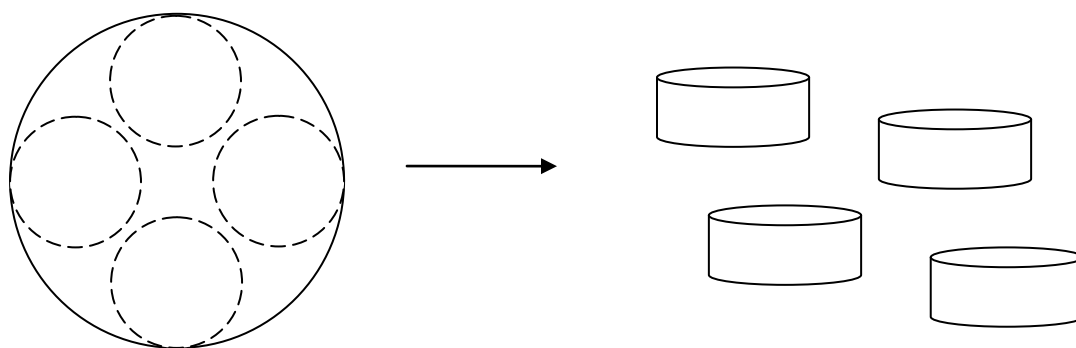


Figure 2: Each well of the 12-well plate produced 4 scaffolds after being cut and removed with cork borer

ESEM and optical microscopy confirm porous morphology. Figure 3 shows ESEM images that reveal a highly porous structure with interconnecting porosity throughout the foam. In each of these images, pores exist on the order of 200 μm .

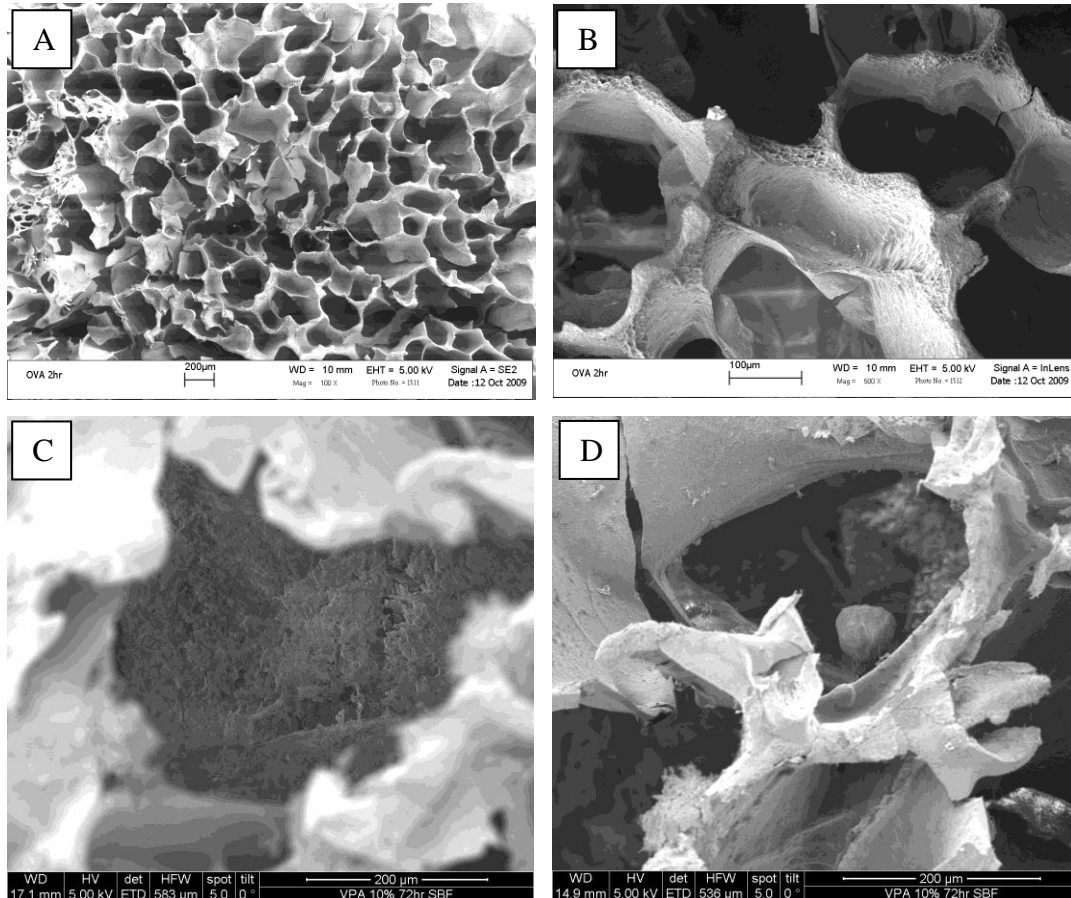


Figure 3: The porosity of ovalbumin scaffolds. (A) Pores cover the entire surface of the material, (B) interconnecting pores can be seen (C) Mineralization seen through a pore on VPA scaffold, (D) Ca-P crystal shown growing inside a pore, with more pores visible in the background

Image (A) above highlights the porosity of the OVA scaffold. Pores acquired through NaCl leaching and freeze drying are visible on the entire surface of the scaffold. Little variance in pore diameter is evident. In images (B) and (D), pores can clearly be seen in multiple layers. Image (C) shows material lying inside of a pore.

Optical microscopy further indicates interconnecting porosity on the order of 200 µm. Pores and pore walls are visible in images taken at 100x (Figure 4).

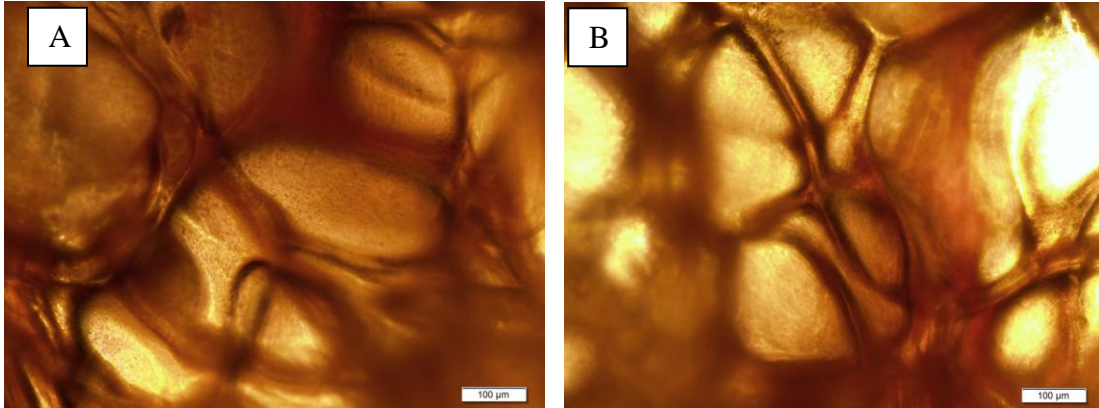


Figure 4: The porosity of ovalbumin scaffolds. (A) Pores cover the entire surface of the material, (B) interconnecting pores can be seen

In both image (A) and (B), bright areas which indicate pores are seen outlined by darker regions indicating the pore walls. Little variance is seen in pore diameter and pore wall thickness. Pore walls are visible both in focus and out of focus, indicating interconnecting porosity.

3.2 Biomineralization

3.2.1 SBF Treatment

OVA scaffolds immersed in 1x SBF yielded no crystallization. Figure 5 below shows an OVA scaffold after 2 hr of incubation with 1x SBF at different magnifications.

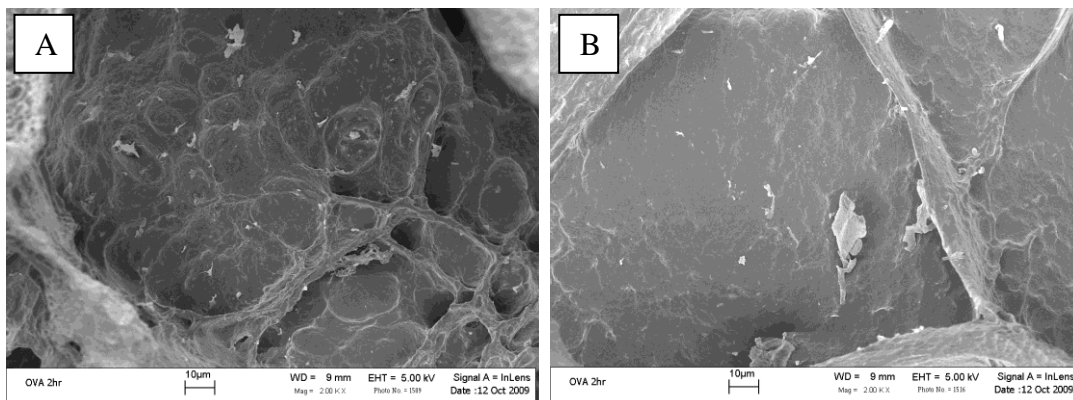


Figure 5: OVA scaffolds after 2 hr immersion in 1x SBF yielded no mineralization

While pore sizes and wall structure are consistent with scaffolds not immersed in SBF, samples appeared visibly damaged.

Although mineralization was not evident from 1x SBF treatments, two scales of Ca-P minerals were seen after treating all scaffold types with 5x SBF. Large, Ca-rich crystals were seen on both OVA and p-OVA (Figure 6).

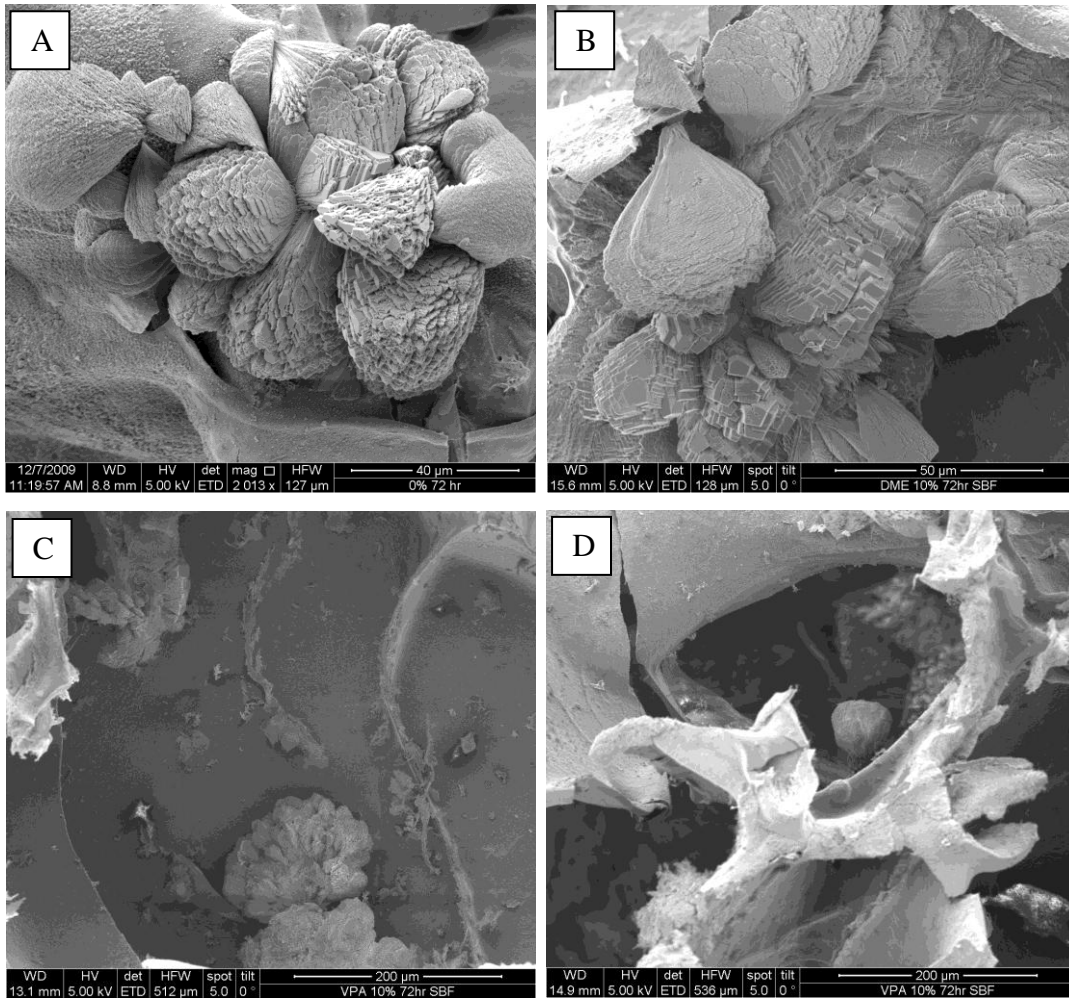


Figure 6: Large-scale Ca-P crystallization on (A) OVA, (B) DME, (C) VPA, and (D) VPA in a pore wall

Each of the large crystals has similar morphologies: flower pedal-like shapes approximately 75-100 μm which grow in and around pores. Small-scale mineralization was only seen on the p-OVA modified scaffolds. Figure 7 below shows (A) an OVA scaffold after

treatment in 1x SBF next to (B) a fracture surface of a p-OVA scaffold after treatment in 5x SBF. In image (A), no crystallization, large or small, is visible. In (B), a thin layer of Ca-P crystallization appears coated on the material's surface, shown in the image to be ranging from 1.2 to 2.7 μm thick. Since the material was fractured after SBF treatment, the thin layer of Ca-P does not appear on the fracture surface itself. No large-scale crystals are visible in this image.

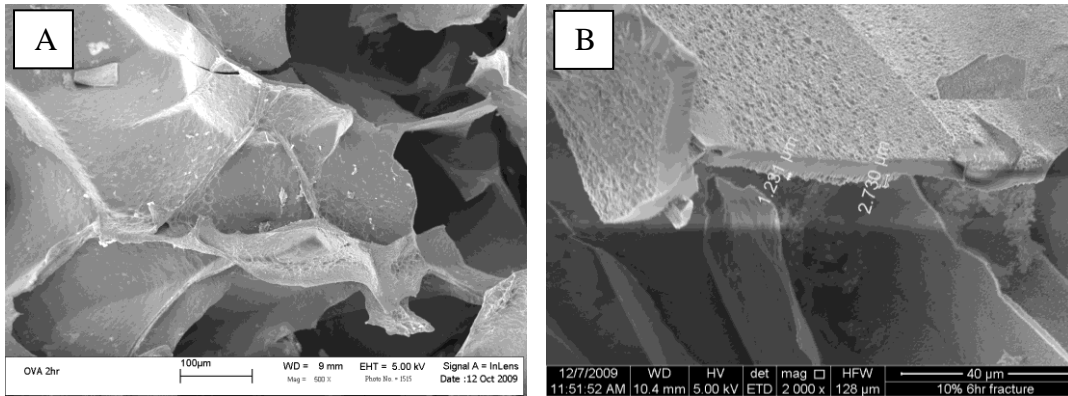


Figure 7: (A) OVA 2 hr after 1x SBF treatment. No Ca-P crystallization seen, (B) p-OVA fracture surface 6 hr after 5x SBF treatment. A thin layer of Ca-P crystals is seen on the surface.

3.2.2 Crystal Growth Profile

Percentage increase in scaffold mass was measured as a function of total time in SBF. Figure 8 shows mass increase as a function of time exposed to 5x SBF for all scaffold types. Each data point represents the average value for a number of scaffolds. The number of scaffolds is not the same for each sample type ($n_{\text{DME,OVA}} = 6$, $n_{\text{BIS } 10} = 4$, $n_{\text{BIS } 20} = 5$) as a result of material processing error.

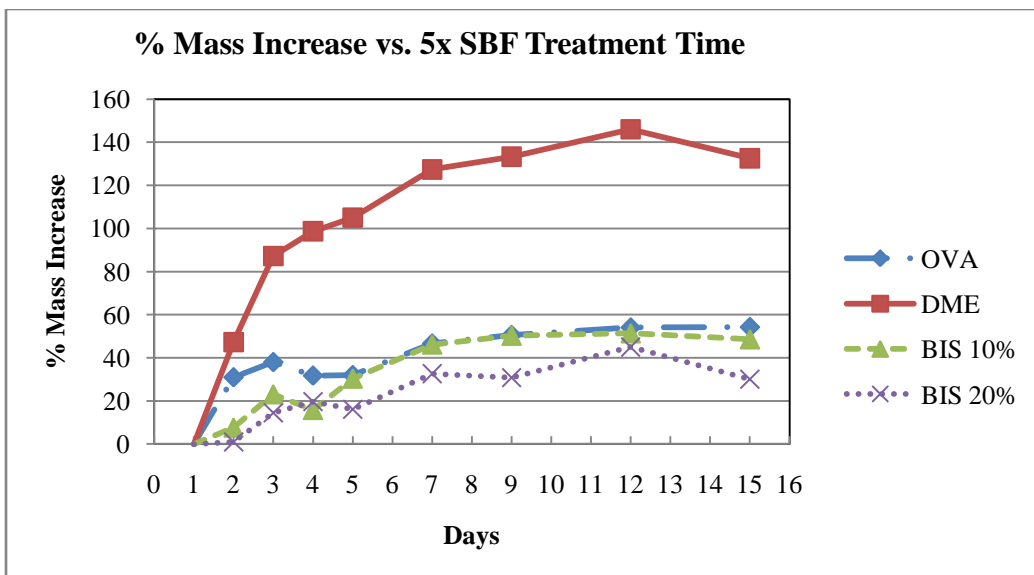


Figure 8: Scaffold mass increase as a function of SBF treatment time

All scaffold types, including unmodified OVA, experienced an increase in mass over time. For the OVA, BIS 10% and BIS 20% scaffolds, a mass gain between 40-60% was experienced. The DME substrate, however, increased in mass nearly 150% over the 15-day period, almost 100% more than any other scaffold type. The rate of mass increase declined with time, as seen by the eyebrow shape of each curve.

ESEM images were taken of the samples at the conclusion of the crystal growth profile study when scaffolds no longer gained weight (Figure 9). Image (A) shows an unmineralized OVA scaffold clearly demonstrating interconnecting porosity. Fully mineralized samples are shown in images (B), (C), and (D).

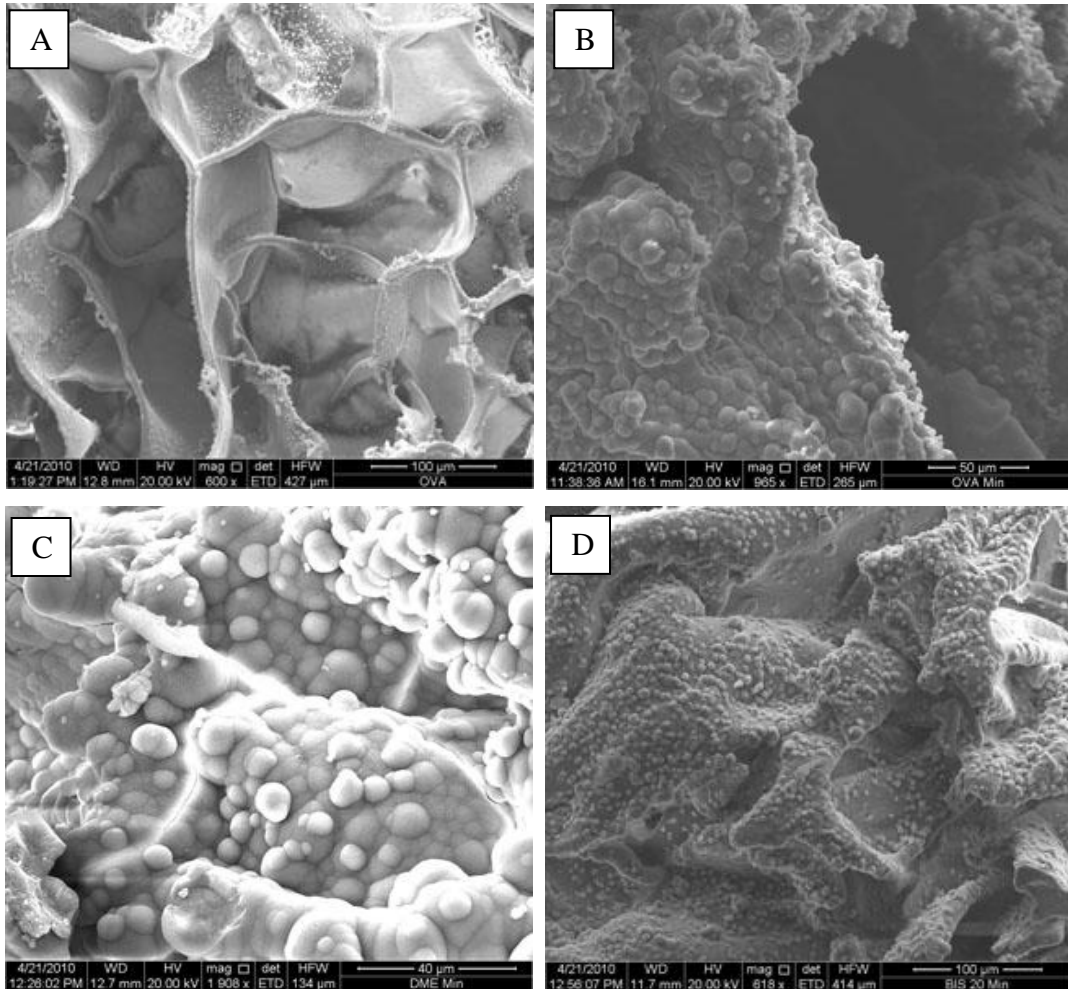


Figure 9: Ca-P crystallization upon completion of crystal growth profile study of (A) unmineralized OVA, (B) mineralized OVA, (C) mineralized DME, and (D) mineralized BIS 20 scaffolds. Total incubation time was 15 days in 5x SBF. Magnifications vary.

Interconnecting pores and pore walls are clearly visible on the unmineralized OVA substrate. While pores are still visible in some locations (B), the vast majority of the surfaces are coated in a layer of crystals. Clearly-defined wall structures are no longer visible, as individual crystals have coagulated to form a thick layer on the OVA and p-OVA surfaces.

3.3 Scaffold Characterization

3.3.1 EDS

EDS scans were performed on crystals to determine elemental composition. In addition to providing an atomic Ca/P ratio with which comparisons to natural bone mineral may be drawn, EDS used in this study featured elemental mapping capable of locating elements on corresponding ESEM images. Scaffolds immersed in 1x SBF did not produce minerals and therefore were not studied.

On the other hand, samples treated with 5x SBF for 72 hr contained large-scale crystals that were scanned with EDS. Figure 10 below shows the spot scanned as well as the elemental composition of the region.

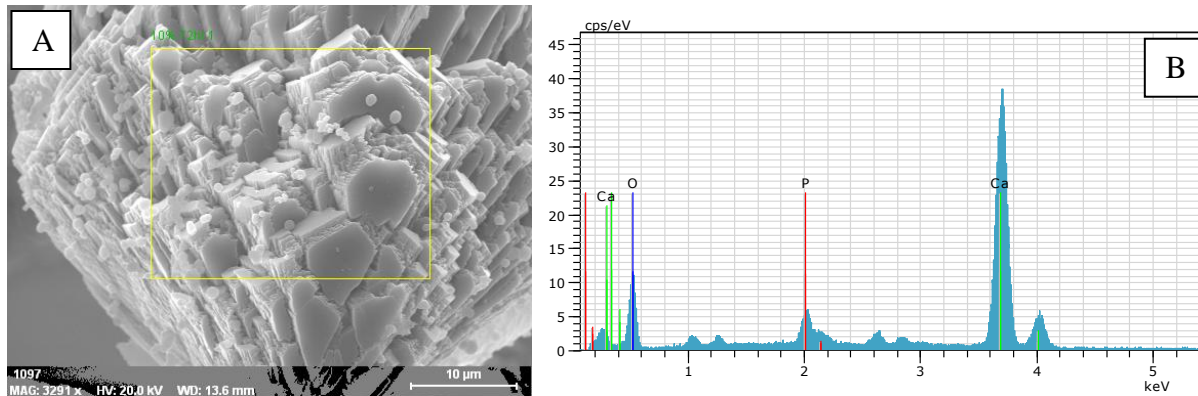


Figure 10: EDS on large-scale crystal after 72 hr incubation in 5x SBF. (A) ESEM image of the spot size scanned, (B) EDS elemental composition of the spot

EDS spectra show the crystal to be Ca-P in nature (B). Crystals present on these scaffolds were heavily Ca-dominant, evidenced by an atomic ratio of 6.73 Ca/P (Table 4). Stoichiometric hydroxyapatite ($\text{Ca}_5(\text{PO}_4)_3\text{OH}$) has 5 calcium atoms for every 3 phosphate atoms, or an atomic Ca/P ratio of 1.67.

Table 4: Elemental composition of large crystal on p-OVA after 72 hr in 5x SBF

Element	Spectrum On crystal
	Atomic %
<i>Calcium</i>	20.85
<i>Phosphorus</i>	3.10
<i>Ca/P Ratio</i>	6.73

The crystal growth profile study required a 15-day immersion in 5x SBF for complete mineralization to occur. At the end of this period when the scaffolds would no longer increase in weight, the samples were examined by ESEM/EDS to determine crystal presence, location, and composition. The following images show unmineralized OVA as well as mineralized OVA, mineralized DME, mineralized BIS 10, and mineralized BIS 20 scaffolds.

Unexpectedly, crystal phases appeared on unmineralized OVA scaffolds (Figure 11). EDS spectra and mapping confirmed this phase to be composed of Na and Cl.

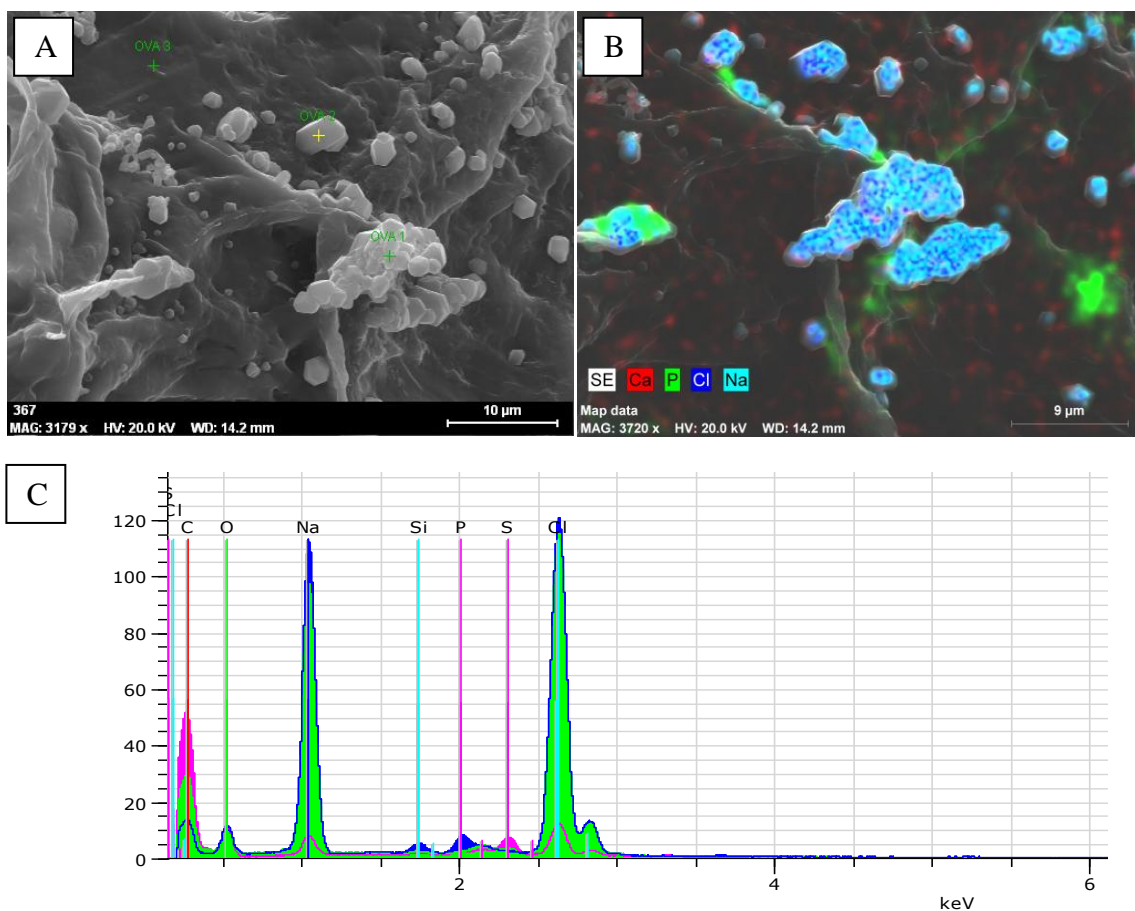


Figure 11: EDS data for unmineralized OVA. (A) ESEM image of scanned spot, (B) Color map locating primarily Na and Cl, (C) Elemental composition of with dominant peaks highlighted

The crystals have a highly notched structure and do not cover the entire OVA surface. EDS mapping in (B) showed both Na and Cl to be present on each crystal, with only trace amounts of P present. Spectra confirm dominance of Na and Cl at scanned locations (Table 5).

Table 5: Elemental composition of scanned spot for unmineralized OVA

Element	Spectrum On Crystals
	Atomic %
<i>Sodium</i>	30.77
<i>Chloride</i>	21.17
<i>Na/Cl Ratio</i>	1.45

Mineralization on OVA scaffolds appeared radically different. In Figure 12 (A), crystals are seen covering the entire scaffold surface. Crystals are composed primarily of Ca and P, as evidenced by EDS mapping in (B).

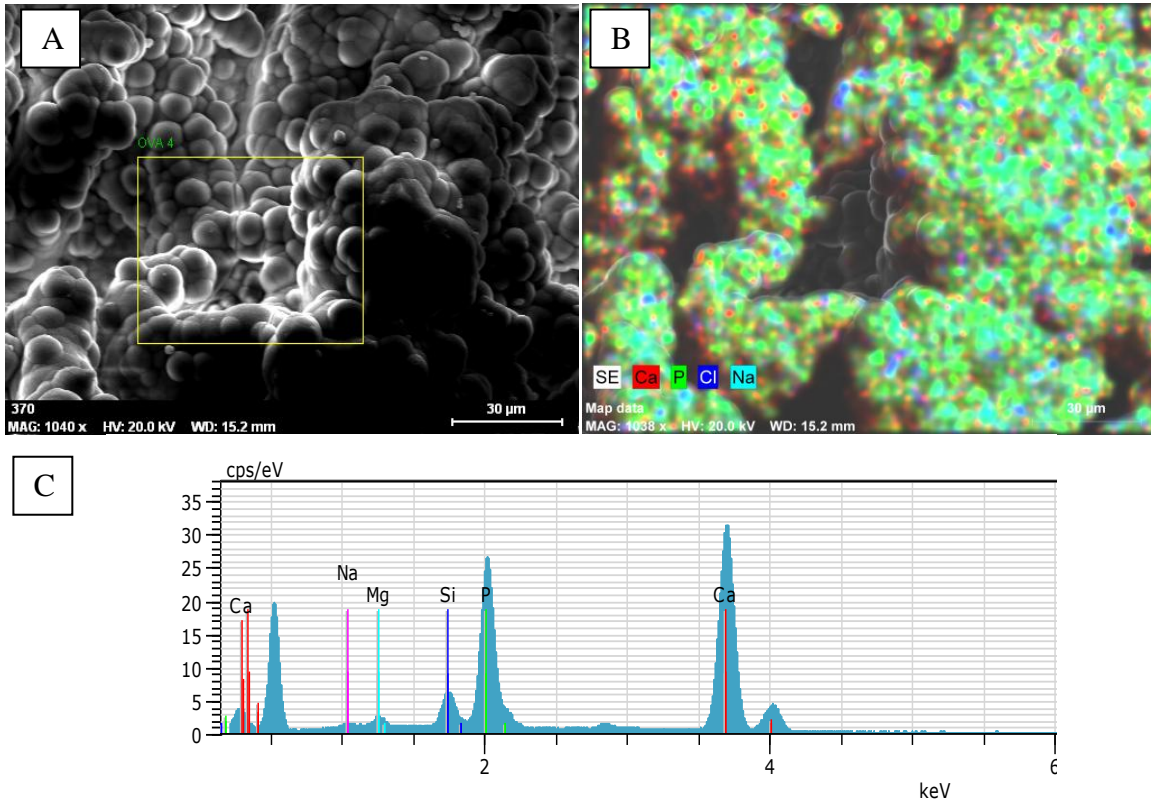


Figure 12: EDS data for mineralized OVA. (A) ESEM image of scanned spot, (B) Color map locating Ca and P, (C) Elemental composition of with dominant peaks highlighted

Furthermore, spectra show that the Ca/P ratio is nearly five times smaller than that seen in samples treated with 5x SBF for 72 hr.

Table 6: Elemental composition of scanned spot for mineralized OVA

Element	Spectrum On Crystals
	Atomic %
<i>Calcium</i>	49.10
<i>Phosphorus</i>	36.28
<i>Ca/P Ratio</i>	1.35

Similar crystallization patterns and morphologies are seen in mineralized DME scaffolds. Again, crystals are seen tightly packed with one another coating the entirety of the surface.

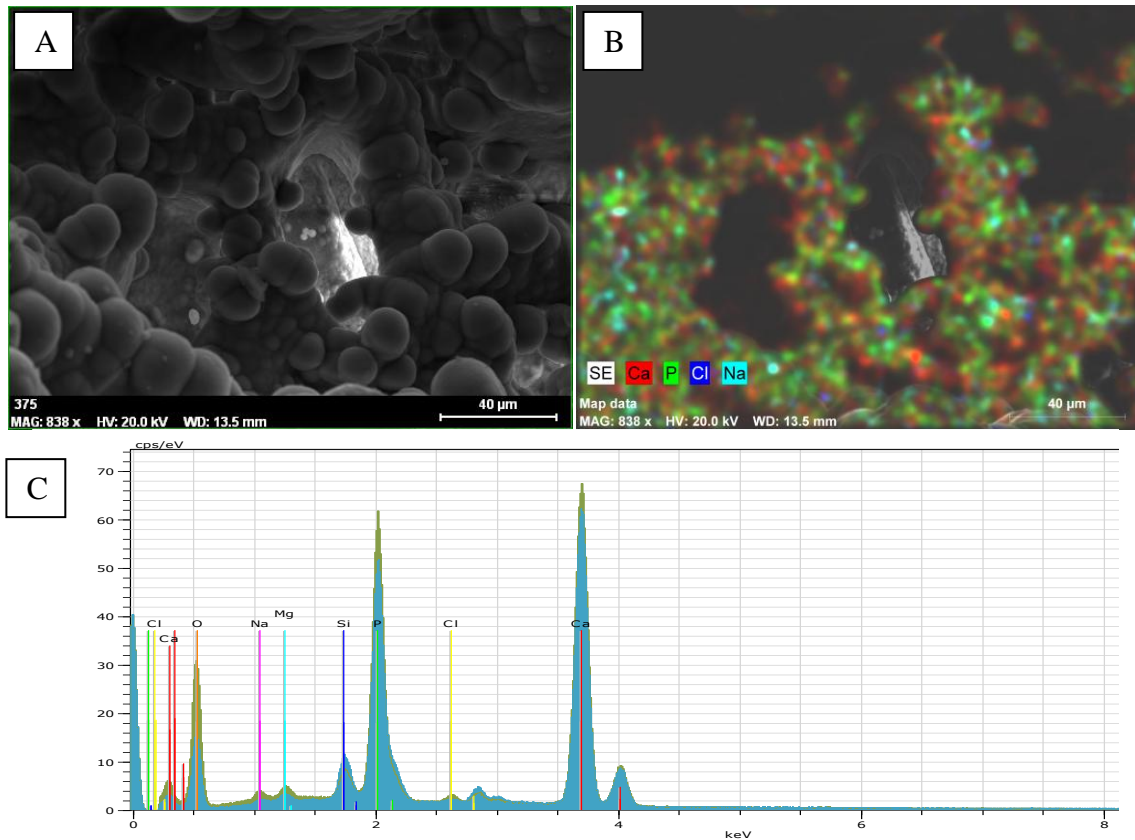


Figure 13: EDS data for DME. (A) ESEM image of scanned spot, (B) Color map locating Ca and P, (C) Elemental composition of crystals with dominant peaks highlighted

EDS mapping, which also identifies two pores, shows crystallization is dominated by Ca and P ions. Spectra confirm Ca-P crystallization, again at a sub-1.67 Ca/P ratio (Table 7).

Table 7: Elemental composition of scanned spot for mineralized DME

Element	Spectrum On Crystals
	Atomic %
<i>Calcium</i>	18.49
<i>Phosphorus</i>	13.80
<i>Ca/P Ratio</i>	1.34

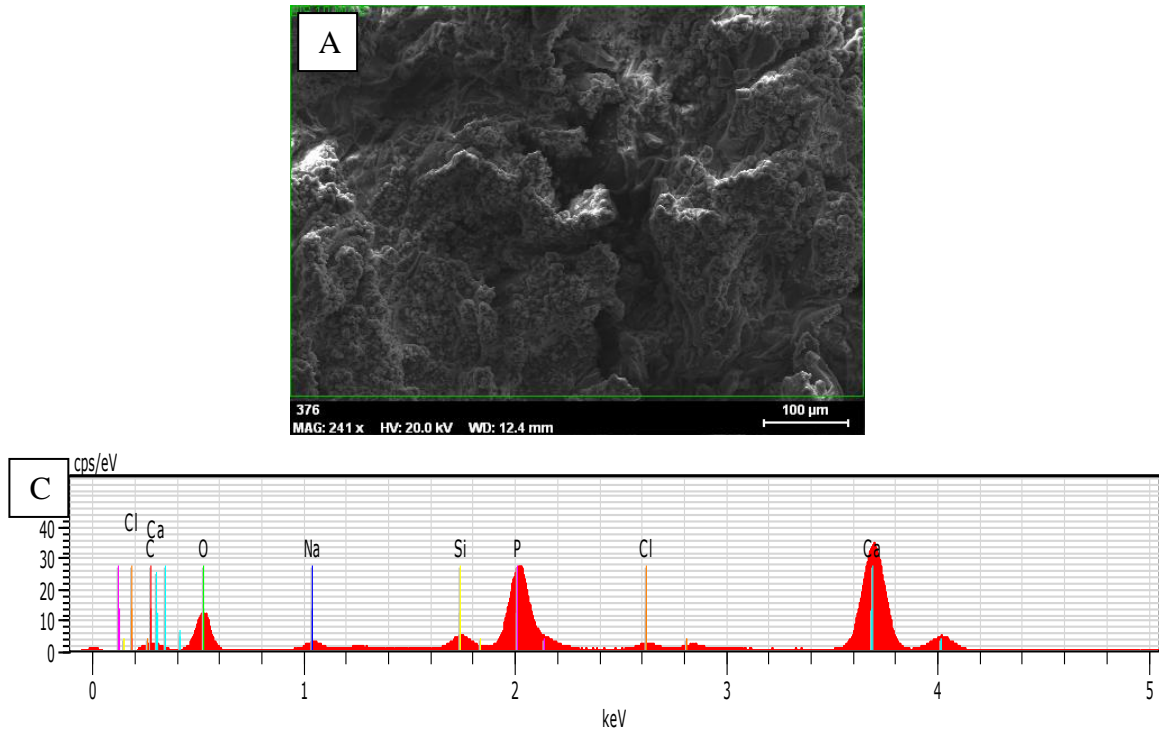


Figure 14: EDS data for mineralized BIS 10. (A) ESEM image of scanned spot, (B) Color map locating Ca and P, (C) Elemental composition of with dominant peaks highlighted

BIS 10 samples exhibited similar crystallization phenomena. While the surface was not as completely coated as in other substrates, much of the surface had been crystallized. Even though EDS mapping was not conducted for this sample, spectra confirm that crystals were composed primarily of Ca and P. The Ca/P ratio of 1.44 was again below that of hydroxyapatite.

Table 8: Elemental composition of scanned spot for mineralized BIS 10

Element	Spectrum On Crystals
	Atomic %
<i>Calcium</i>	15.28
<i>Phosphorus</i>	10.63
<i>Ca/P Ratio</i>	1.44

Mineralization on BIS 20 was consistent with other substrates as well.

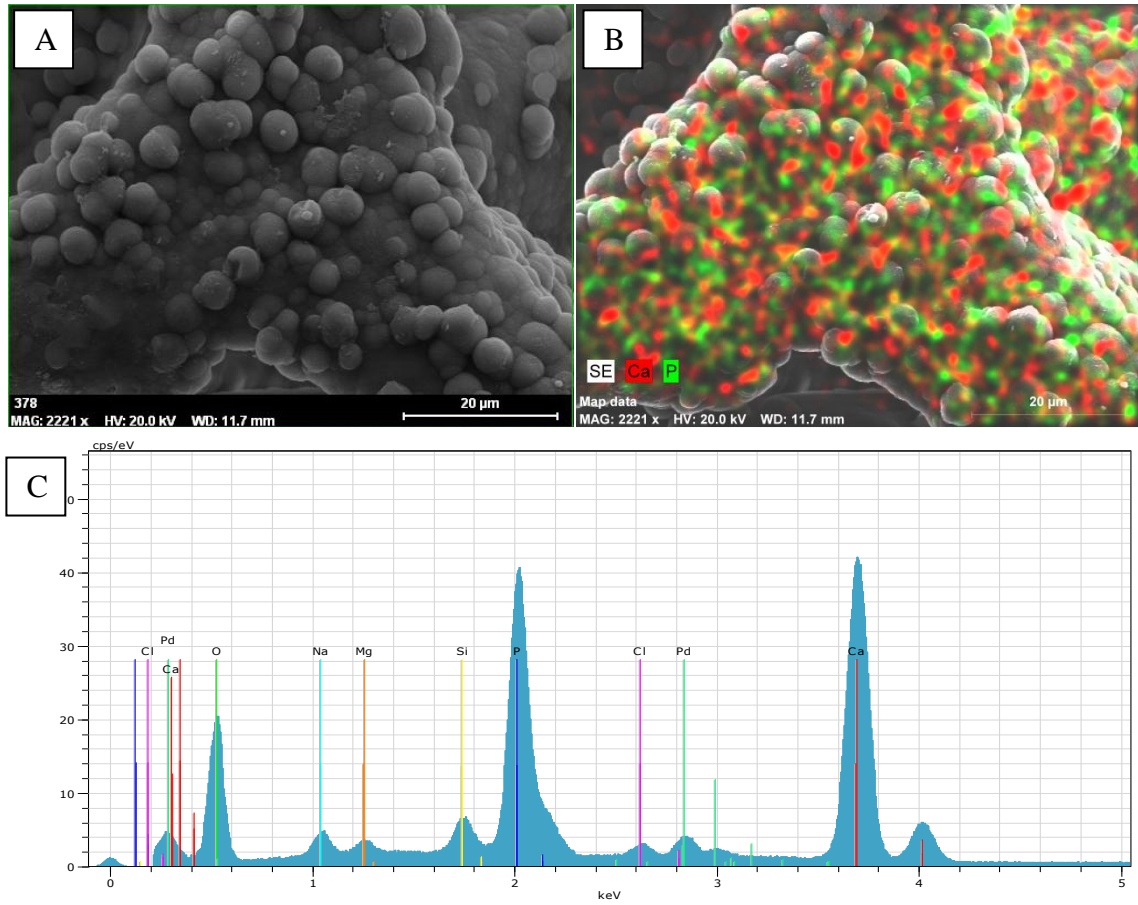


Figure 15: EDS data for BIS 20. (A) ESEM image of scanned spot, (B) Color map locating Ca and P, (C) Elemental composition of with dominant peaks highlighted

As on other scaffolds, trace amounts of Na, Cl, Mg, Si, and Pd were all visible in EDS spectra but were not dominant in elemental mapping. While crystals appeared to have similar morphologies, the Ca/P ratio on BIS 20 was only 1.15.

Table 9: Elemental composition of scanned spot for mineralized BIS 20

Element	Spectrum On Crystals
	Atomic %
<i>Calcium</i>	14.16
<i>Phosphorus</i>	12.32
<i>Ca/P Ratio</i>	1.15

3.3.2 Mechanical Testing

Rheology was used to test the gel-like behavior of the OVA and p-OVA scaffold types.

Both mineralized and unmineralized samples were tested in each case.

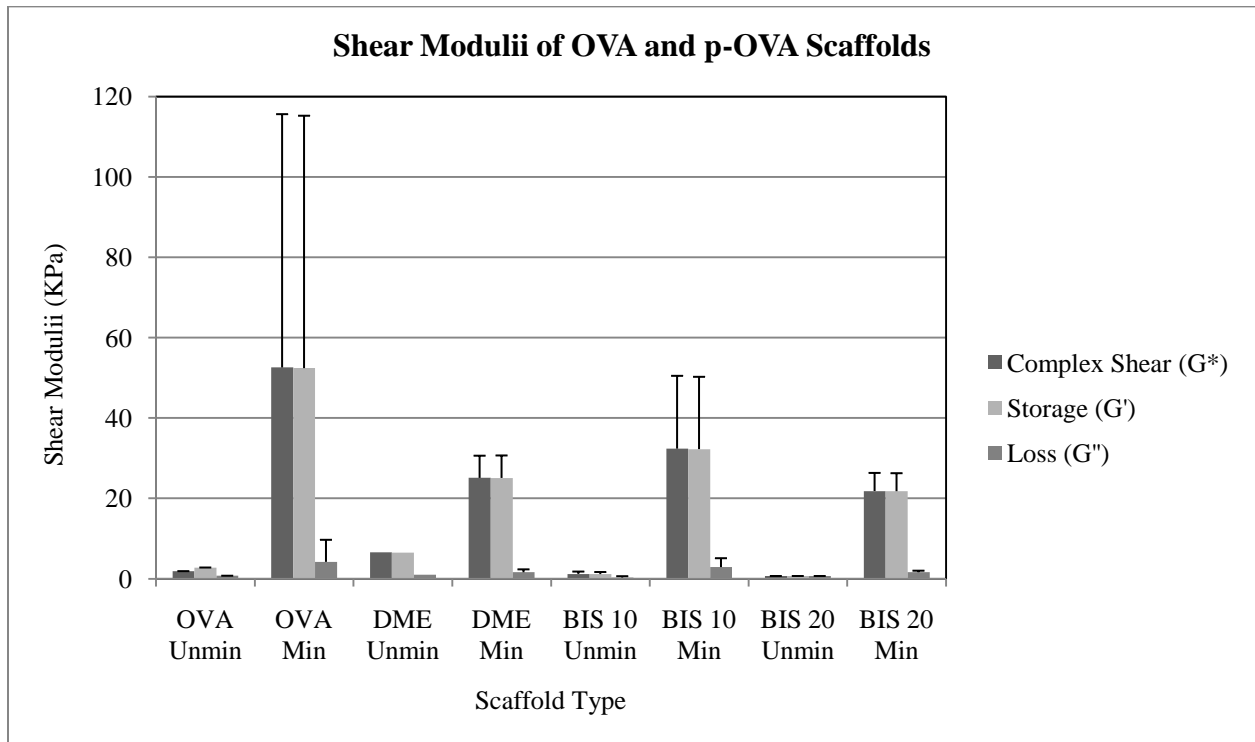


Figure 16: Rheology data shows mineralized samples have stronger complex shear moduli than unmineralized counterparts

As evidenced in the above graph, average complex shear moduli values ranged from 1 – 53 KPa. The lowest values appeared for the unmineralized BIS samples, while the highest values appeared for the mineralized OVA samples. For a given substrate type, the mineralized scaffolds always had a higher complex shear modulus than unmineralized counterparts.

3.3.3 Degradation

Weight loss as a function of time is measured in Figure 17 below. Since samples were first introduced to PBS+collagenase XI in the dry state, percent weight loss was measured from day 3, allowing adequate time for samples to swell to maximum weight.

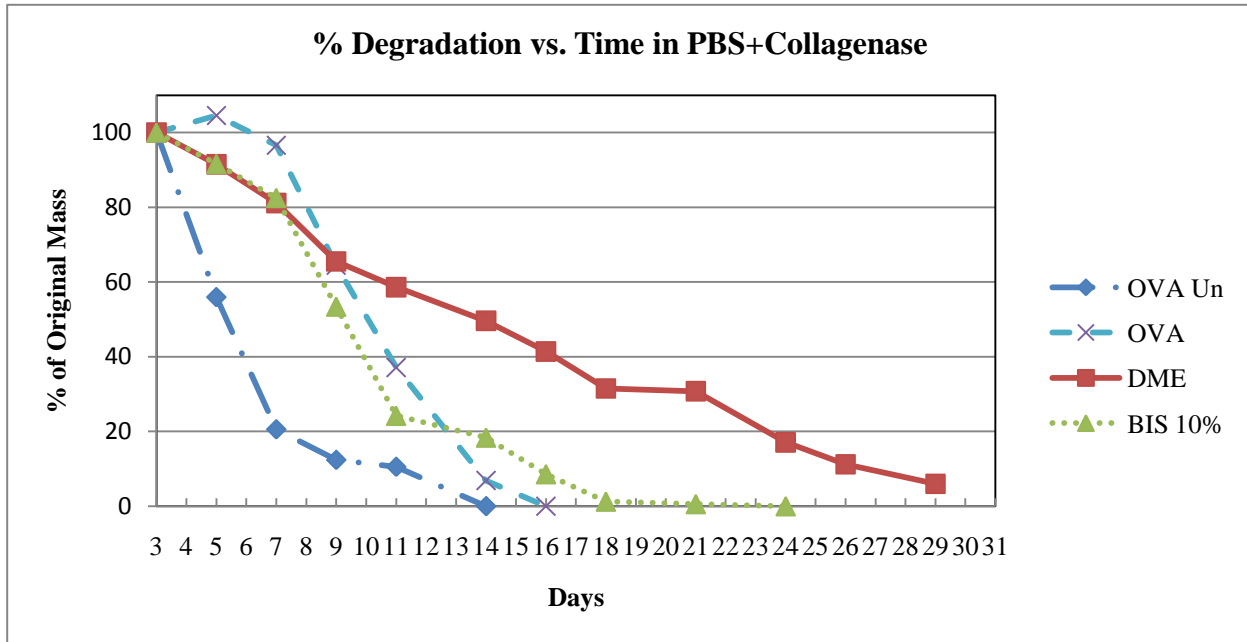


Figure 17: Degradation in PBS+Collagenase XI shows mineralization prolongs time to complete degradation

Degradation times varied for all substrates. The unmineralized OVA scaffolds degraded the quickest, completely disappearing within 9 days. Mineralized OVA scaffolds degraded after 17 days. After 24 days, the BIS 10 scaffolds fully degraded. As of 29 days, mineralized DME scaffolds degraded nearly 95%.

Unmineralized OVA lost 80% of its mass in the first week of contact in PBS+collagenase XI. However, the last 20% did not degrade for another full week. Similar patterns are seen in other samples as well: while not as evident in mineralized OVA, mineralized BIS 10 shows a sharp decline in mass over the first 11 days, then requires 13 more days for the final 20% to

degrade. This trend is recognizable but not as pronounced for mineralized DME scaffolds. If extrapolated from day 9, complete degradation would not be expected until day 20. However, more than 5% of the scaffold mass remained more than a week past that time.

3.4 *In Vitro* Cell Studies

3.4.1 *Live/Dead Assay*

The live/dead combined assay was run to determine how many cells seeded onto each scaffold type lived and how many died. In the following images, cells that appear green and demonstrate a proper morphology are alive, whereas any cells that appear red are dead. Images below are representative of overall cellular viability. Since no dead cells are seen in any images, viability is roughly 100% for all scaffold types after 24 hr incubation.

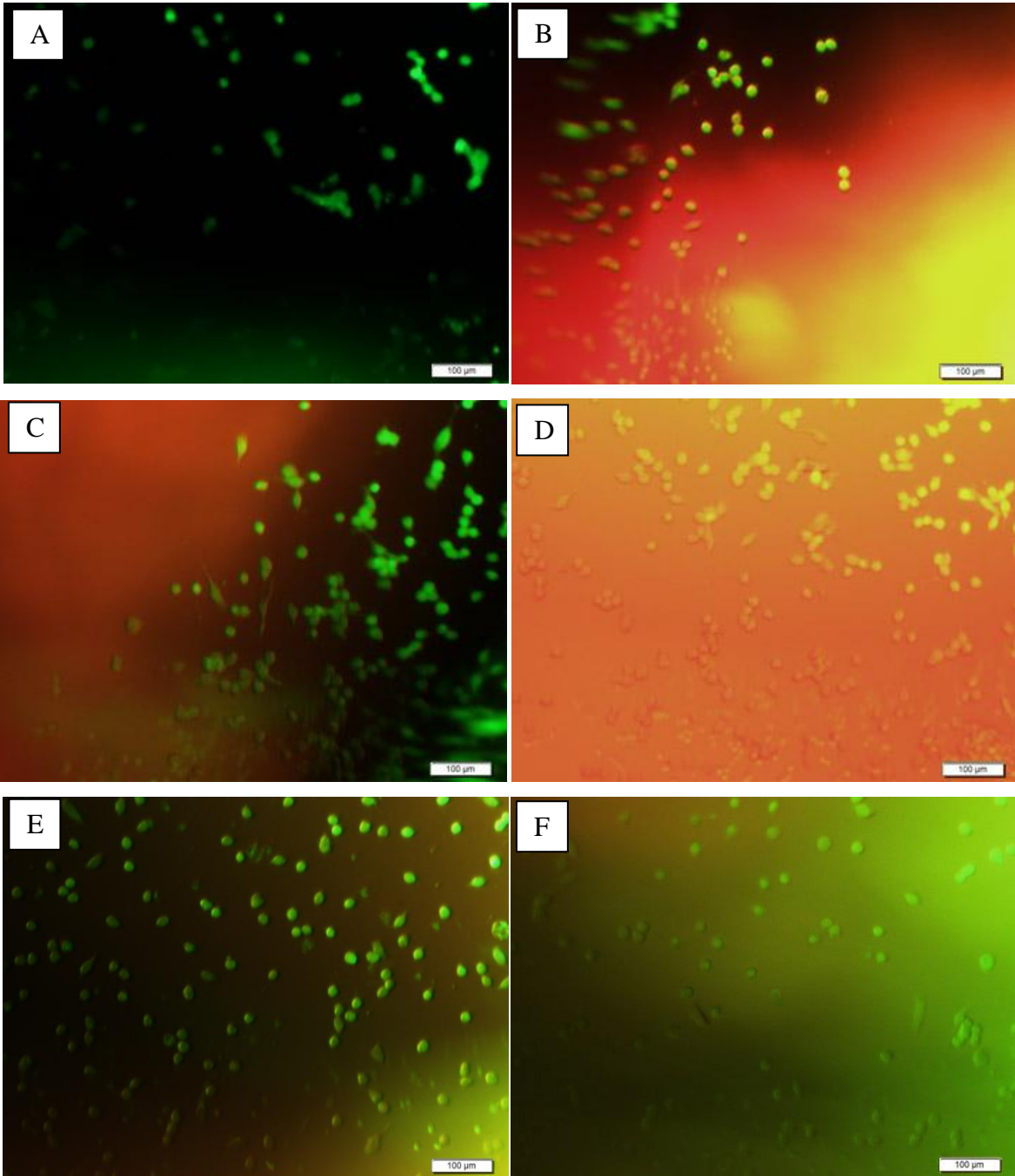


Figure 18: Combined live/dead images of (A) Unmineralized OVA, (B) Mineralized OVA, (C) Unmineralized DME, (D) Mineralized DME, (E) Unmineralized BIS 10, and (F) Mineralized BIS 10 scaffolds

3.4.2 Cell Proliferation – MTT Assay

MTT was performed for 1 and 3 day time periods. Cell number was obtained, however the data was inconclusive.

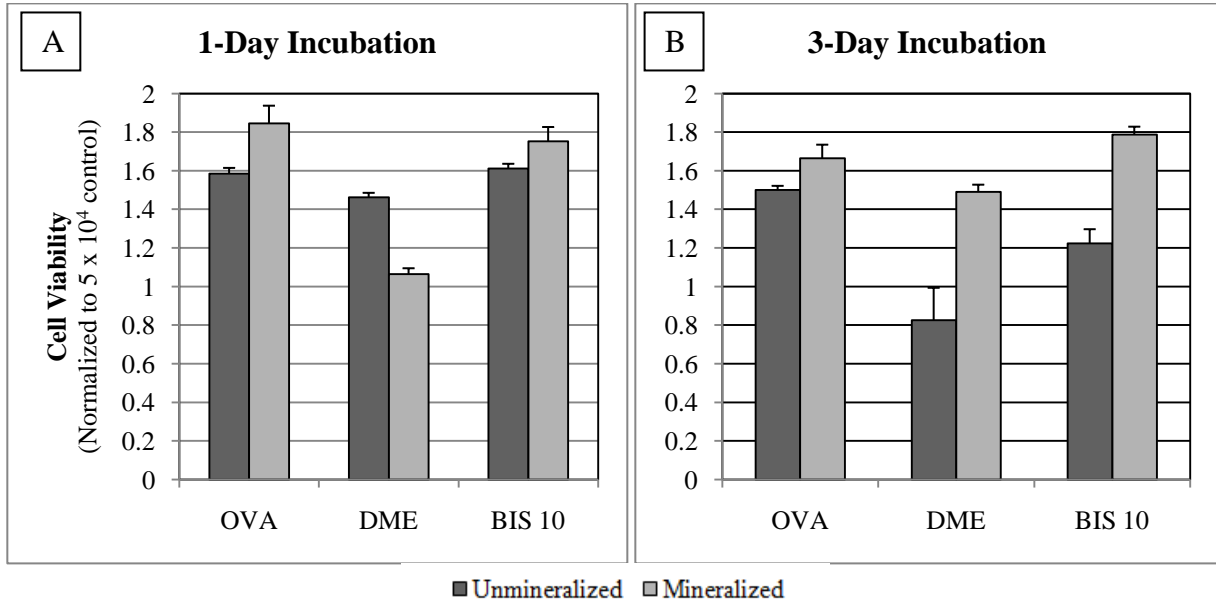


Figure 19: Variation in MTT assay results in inconclusive data for (A) 1-day incubation and (B) 3-day incubation times

Data presented in Figure 19 is normalized to the 50,000 cell control triplicate.

Chapter 4: Discussion

4.1 Scaffold Design and Fabrication

The successful crosslinking of OVA scaffolds resulting in a three-dimensional porous structure was expected. Farrar determined in past studies that ovalbumin scaffolds could be crosslinked with varying amounts of GA. However, the amounts used were all in excess of what the reaction required. Even though the reaction was stopped using a 0.1 M glycine solution, it could not be determined based on that study whether or not OVA scaffolds required all 19 lysine groups per chain to crosslink the material [51]. Seeing the same structure in p-OVA scaffolds despite reducing the number of lysine groups available for crosslinking indicates that not all lysine groups were required for successful crosslinking. Phosphorylation added phosphate groups on the amines of the lysine groups, rendering them incapable of reacting with GA. The Michael addition reaction utilized seven of the 19 lysine groups per chain for phosphate conversion, leaving 12 unmodified lysine groups per chain for GA crosslinking. While the number of converted lysines was not directly measured, the reaction itself is considered precise.

4.2 Biomineralization

4.2.1 SBF Treatment

During the pilot study in which OVA scaffolds were immersed in 1x SBF for one week, OVA samples appeared visibly damaged. Low magnifications showed damage to the pore walls, and areas of the scaffolds appeared cratered at higher magnifications (Figure 20).

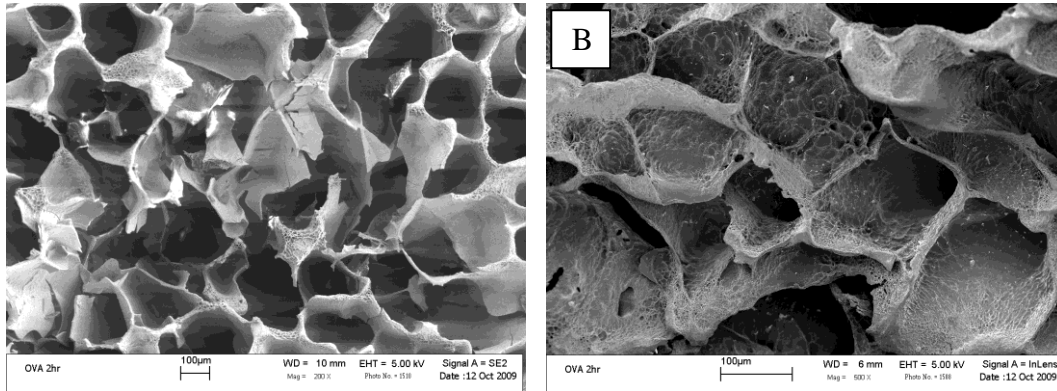


Figure 20: (A) OVA 2 hr after 1x SBF treatment. No Ca-P crystallization seen, (B) OVA surface showing water damage

It was found that the OVA samples that appeared damaged had not been fully frozen before freeze drying. The ice crystals that are normally sublimed by freeze drying were therefore water droplets that boiled off the OVA surface. Crater marks were left in place of the evaporating water. Care was taken to avoid this phenomenon in later work. The damage seen in these scaffolds is not believed to be the cause for the lack of mineralization.

Variables such as scaffold surface charge, pH of SBF, and scaffold surface area to volume of SBF ratio are all factors that may have contributed to the lack of mineralization seen [43]. The ionic nature of SBF requires that a surface charge exists for Ca and P ions to precipitate onto the scaffold. If no such charge exists, these ions may come together and precipitate out of solution, but chemical bonds do not form between the crystal and the scaffold, causing simple rinsing procedures to detach the crystals. Incorporating a surface charge via phosphonates increases the likelihood that precipitated ions chemically bond to the p-OVA surface and contribute to mechanical strengthening in multiple loading conditions.

These variables were taken into consideration while conducting 5x SBF experiments. There is a slight difference in the pH of 1x and 5x SBF. As noted in Table 2, the pH of 1x SBF is 7.4, while the pH of 5x SBF is 6.8. While small, the difference in hydrogen concentration can

determine whether negatively-charged OH^- groups bind to crystals, however slow this process may be. Any added negative charge to individual crystals would theoretically enable more positively-charged Ca ions to attach, although electrostatic interactions must be considered as well. During the crystal growth profile, the ratio of the surface area of the scaffold to the volume of SBF was altered. Six scaffolds were placed in 60 mL 5x SBF as opposed to two scaffolds placed in 10 mL 5x SBF as before. Individual scaffolds were able to interact with twice as many ions, allowing complete mineralization in 15 days.

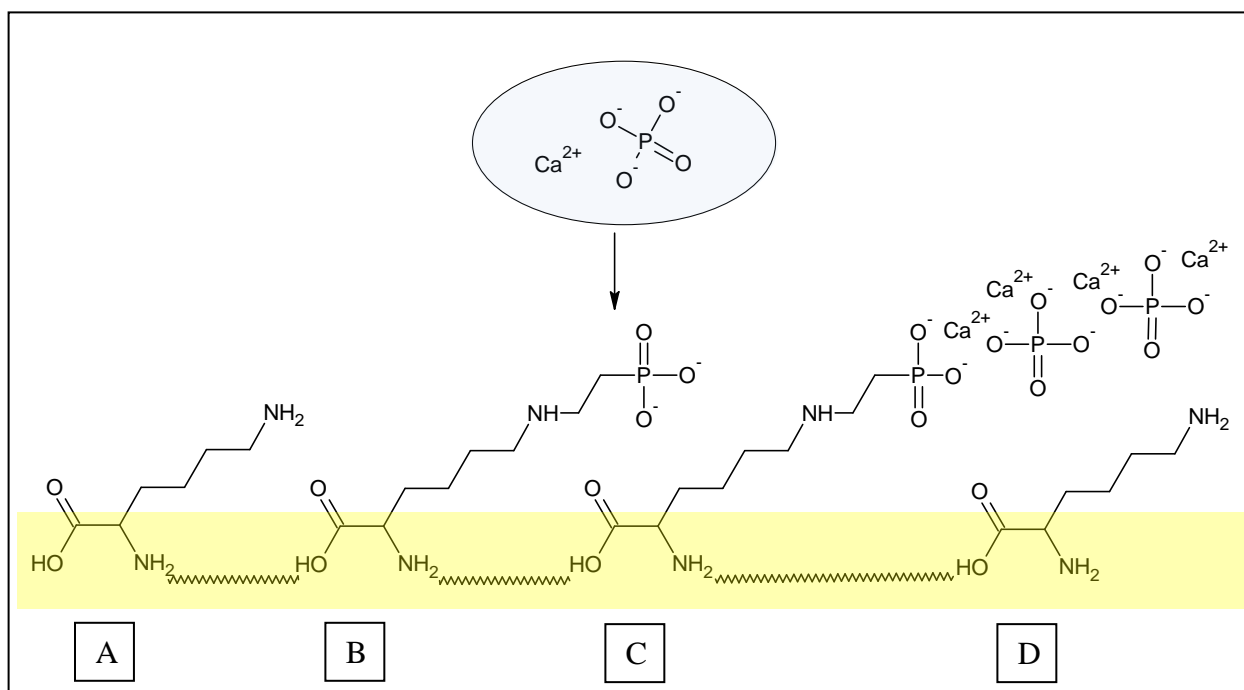


Figure 21: Schematic illustrating mineralization of a VPA scaffold

Figure 21 above illustrates the phosphorylation and mineralization sequence of scaffolds exposed to SBF. The OVA backbone is shown highlighted in yellow, depicted chemically by the chain interconnecting the amino acids. An unmodified lysine group is shown at (A). This lysine will not interact chemically with SBF within an acceptable timeframe. A phosphonated lysine

group is shown in (B). It is evident based on the R group that the substrate in this example is VPA. This group serves as a nucleation site for calcium phosphate crystallization. A calcium ion and a phosphate group are shown in a droplet of SBF, highlighted in blue. These ions are drawn to the nucleation site, shown by the downward-pointing arrow. At (C), a Ca-P crystal has formed. Finally, (D) represents another unmodified lysine group, indicating that not every lysine group is phosphonated. The actual percentage of modified groups is less than 10% for all substrates with the exception of BIS 20%.

4.2.2 Crystal Growth Profile

All scaffold types, including unmodified OVA, gained mass as incubation time in SBF increased. For the OVA, BIS 10% and BIS 20% scaffold types, a mass gain of 40-60% was seen. The DME substrate, however, increased in mass nearly 150% over the 15-day period. It is interesting to note that the OVA substrate did not experience the least amount of weight gain as expected. Modifications to the OVA substrate were performed with the intent of enhancing the material's ability to nucleate and grow Ca-P crystals, yet the data shown in the weight gain experiment show otherwise. Both the BIS 10% and BIS 20% scaffolds experienced a smaller percent increase in weight.

Electrostatic interactions may play an important role in the degree of mineralization seen on various OVA surfaces. Since each modification changes the ovalbumin surface charge, it is plausible that modifying the lysine groups to too great of an extent can have a negative effect on the amount of mineralization seen. This would be the case for both BIS substrates. While an individual phosphonate provides a nucleation site for Ca-P crystallization, adding two phosphonates on the same lysine may not provide enough physical space for Ca and P to bind.

However, since mineralization was seen on both BIS substrates, it is also possible that bisphosphonates do allow mineralization, but do not provide as much space for growth as other substrates. Since over 90% of the lysines in BIS 10 were unaltered, mineralization would still be seen, but not to the extent seen on other substrates.

The crystal growth profile also provides information regarding the kinetics of the 5x SBF interaction with scaffolds. Each of the mass gain curves initially demonstrates rapid crystal growth, and then shows a leveling-off over time. This would suggest that as Ca and P are initially gathered on the scaffold surface, a large number of nucleation sites are available for crystal growth. As time progresses and SBF is changed, the number of available sites decreases and the ions in SBF are no longer able to interact with the scaffolds directly. While some ions attach to other crystals and contribute to crystal growth, the decline in nucleation sites contributes to the slowing of the growth, and therefore the leveling-off of the mass gain curves. Eventually, crystals coalesce and grow to a point where further growth is no longer thermodynamically favorable, and no further mass is gained.

Unexpectedly, NaCl salt crystals appeared on OVA samples that were not exposed to SBF. The DI water rinse following glycine rinse during scaffold fabrication was designed to eradicate NaCl presence after pores had been created. Salt crystal diameter is significantly smaller than the initial 150 μm , meaning dissolution occurred but never completed. Traces of Na and Cl are also seen in samples that were exposed to SBF. While SBF does contain a large amount of these ions, the possibility exists that NaCl porogen remained on the scaffold surfaces prior to Ca-P nucleation and growth. Care should therefore be taken in future studies to fully wash samples in DI water prior to biomineralization.

4.3 Scaffold Characterization

4.3.1 Mechanical Testing – Rheology

Rheology studies were conducted to characterize the scaffolds' mechanical strength. Since OVA and p-OVA scaffolds are hydrogels, rheology accurately measures both elastic and viscoelastic response in the wet state at body temperature, or *in situ*. After running the rheological tests, the data shows that for a given substrate type, the mineralized scaffolds always had an increased complex shear modulus compared to unmineralized scaffolds. Unmineralized samples deformed easier than the mineralized samples under a given shear load. This strongly suggests that the strengthening effect of Ca-P mineralization outweighs any weakening effect seen due to chemical modification to the scaffolds despite reducing the number of available crosslinking sites. With the exception of a possible outlier in the mineralized OVA case, each material experienced a similar increase in complex shear modulus. It cannot be determined from this test alone which substrate modification provides the highest degree of mechanical improvement.

A question that remains untested is whether the improvement to mechanical strength is enough to prevent the material from failing prematurely *in vivo*. Since natural bone can have a shear modulus as high as 5 GPa, it would be desirable for the OVA and p-OVA scaffolds to possess this same strength to minimize stress concentration [52]. Even with mineralization, the shear moduli of the scaffolds are still orders of magnitude weaker than trabecular bone. Considering bone is under a constant remodeling process as cells permeate the material and the scaffolds undergo degradation over time, quantifying lower limits on strength is difficult [53].

4.3.2 Mechanical Testing – Degradation Study

Complete degradation of the scaffolds required only three weeks for all scaffold types. Time to degradation was accelerated compared to previous studies on OVA; in Farrar's work, OVA scaffolds required 5 weeks to degrade whereas results indicate only 2 weeks were required in this study [30]. Procedures used in this experiment were modeled after previous work with the exception of enzymes chosen. The environment simulated by 1 mg/mL PBS+collagenase XI is much more concentrated than those experienced anywhere in the human body, whereas those simulated by 1 mg/mL PBS+collagenase I model conditions of an arthritic knee [54]. Collagenase XI is rated at >1,200 collagenase digestive units (CDUs) whereas collagenase I is rated at >125 (Sigma). In other words, type XI liberates over ten times more peptides than type I under the same experimental conditions. Thus, experimental degradation time does not reflect or model *in vivo* degradation time. Instead, the relative degradation rates between mineralized and unmineralized scaffolds are of importance. Because the degradation environment was identical for all scaffold types, it can be concluded that mineralized samples are more resistant to degradation and would require more time to dissolve *in vivo*.

While no degradation byproduct is toxic for either OVA or p-OVA scaffolds, the allergenic nature of OVA is a concern for patients with egg allergy. OVA is the primary allergen in egg white responsible for egg allergies in humans [55, 56]. Even though methods of eradicating allergic response have been researched and that influenza vaccines have been administered to patients with egg allergies with minimal allergic response, care should be taken when implanting OVA scaffolds [55, 57].

4.4 *In Vitro* Cell Studies

4.4.1 *Live/Dead Assay*

Fluorescent images confirm cells survived on each scaffold type. A difficult aspect of the live/dead assay was OVA's autofluorescence at both the green and red wavelengths (Figure 22).

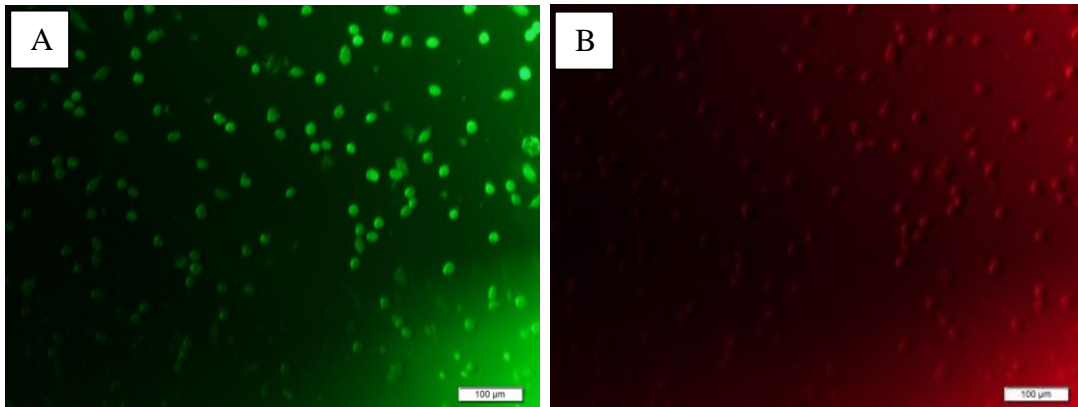


Figure 22: (A) Live stain on unmineralized BIS 10. All cells are viable, as indicated by green stain. Image (B) shows scaffold autofluorescence causes these same cells to be visible with the dead stain despite being viable.

Fluorescent microscopy of the live stain results in all cells appearing viable. These cells should not appear in the dead stain, yet they do. Autofluorescence of the scaffolds caused viable cells to be visible but unstained at the dead fluorescent wavelength. Combining the images revealed that the cells were viable based on both color and morphology (Figure 18). Since no dead cells were detected after 24 hr, viability can be approximated at 100% for all scaffold types, although that number is subject to change at longer incubation times.

4.4.2 *Cytotoxicity – MTT Assay*

Cytotoxicity measurements via MTT results were inconclusive. Since cells were incubated in sterile D-MEM in this study, low cell splitting was expected due to the lack of growth factors typically provided by FBS [58, 59]. Any mitosis would be the direct result of cell

interaction with Ca-P crystals, and not the result of nutrients in media. Therefore, absorbance values measured greater than the control wells (any value greater than 1) indicate one of two possibilities: cells proliferated on the scaffolds as a result of interaction with Ca-P crystals, or microscopic OVA fragments remained in the well plates after scaffolds were removed. Since live/dead images were taken after scaffold removal and fragments still appeared, the latter effect is feasible. In such a case, light would be heavily absorbed by fragments, leading to a falsely high absorbance reading.

The morphology of the scaffolds is the more probable source of inconsistency in MTT data reported in this study. All scaffold types that were seeded with cells appeared to be thoroughly stained purple after the four hour incubation with MTT at both 1-day and 3-day time points. Normally, the purple crystals formed by viable cells are dissolved in solubilization solution and turn the measured solution yellow. In this study, however, the scaffolds remained purple even after adding the solubilization solution. It is likely that not all formazan crystals were dissolved and therefore the full contribution of viable cells was not measured. The three-dimensional porous structure of the scaffolds may have contributed to the inability of the solubilization solution to affect the purple formazan crystals. Any cells that infiltrated deep into the scaffolds may not have been lysed by the solubilization solution and therefore may not have released formazan crystals. Furthermore, the purple crystals may have been trapped in the scaffold structure once formed. In any case, destroying the scaffold structure prior to adding solubilization solution may aid in the release and dissolution of formazan crystals. Transferring this solution to a new well plate should avoid false absorbance due to scaffold fragments as well.

Chapter 5: Conclusions

Previous research has shown OVA bone scaffolds to have a morphology and structure conducive to osteoblast adhesion. These viable scaffolds were also shown to degrade in the body in a 6 – 8 week period of time. The limiting property of the scaffolds is their mechanical strength. This study presented a method of biomineralization intended to enhance the mechanical integrity of the scaffolds without harming interaction with osteoblasts. In doing so, both OVA and p-OVA scaffolds were immersed in 1x and 5x SBF solutions for varying amounts of time. The mechanical and cellular response was measured to determine whether an improvement was made to the unmineralized scaffolds studied before.

As shown in past research, OVA scaffolds were successfully crosslinked. Modifications to the structure of OVA were performed with the intent of enhancing the material's ability to nucleate and grow Ca-P crystals. This modification did not inhibit GA crosslinking; p-OVA scaffolds were successfully crosslinked as well despite losing lysine groups to phosphorylation.

Biomineralization was achieved on all OVA and p-OVA substrates. Immersion in 1x SBF was rejected early since it did not yield a substantial amount of mineralization. During 5x SBF treatments, all substrates experienced an increase in weight due to Ca-P mineralization. This mineralization was observed by FESEM images and was detected by EDS measurements as well. While the DME modification increased in mass by over 130%, the p-OVA scaffold types did not all produce more crystallization than unmodified OVA. Instead, it was found that altering surface charge affected the amount of mineralization seen.

Mechanical studies were performed to determine any strengthening effect of Ca-P minerals on the OVA and p-OVA scaffolds. Rheology showed that mineralization caused an order of magnitude increase in the complex shear modulus of each scaffold type. A degradation

study using PBS and collagenase type XI revealed that the minerals caused the time required for full degradation to increase by up to two weeks.

Cellular studies were conducted to determine effects of Ca-P mineralization on cytotoxicity. Live/dead staining showed that cells survived in the area surrounding all scaffold types, indicating Ca-P minerals were not directly toxic to osteoblasts. The MTT assay quantified cytotoxicity levels and showed no significant difference between unmineralized and mineralized scaffold types.

While this study has not conclusively shown that the Ca-P mineralization of OVA and p-OVA scaffolds enhances mechanical and cellular response, all data recovered up to this point would indicate trends in that direction. As additional tests are performed and more data is gathered, the accuracy of initial indications provided by this study will become clearer. It is conclusive, however, that Ca-P crystallization is achievable using 5x SBF biomineralization treatments, and that the amount of crystallization seen can be improved by selective phosphorylation of excess lysine groups.

5.1 Future Work

Future work should focus on optimizing the processing techniques used in this study so that consistent mechanical and cellular responses can be measured and evaluated. For the biomineralization process, adjustments can be made to Ca and P concentrations in SBF since mineral deposits on completely mineralized scaffolds were calcium-deficient compared to HA. Another limitation was modifying only 10% of the OVA structure for each p-OVA material. In other words, p-OVA solution was mixed with unmodified OVA solution to result in 10% v/v modification, with the sole exception being BIS 20. Learning the effect of degree of modification could help solidify observations noted in this study regarding the proposed

mechanism of mineralization. Furthermore, it is unknown whether the internal scaffold structure was mineralized; micro-CT imaging could locate any such crystals. A method could be developed to obtain an XRD reading of crystallization compared to pure scaffolds, since it is difficult to identify specific crystal phases present without such data. Mechanically, mineralized and unmineralized scaffolds can be tested in a different loading condition (tensile, compressive) to further characterize response and to contribute to statistical significance. Additional cells studies can be performed to further analyze cell-scaffold interactions, specifically differentiation or gene expression tests. The effect of mineralization on cell infiltration throughout scaffolds could also be studied. With this information, the future of mineralized OVA and p-OVA as bone scaffold materials can be realized.

Chapter 6: References

1. Wraighte, P.J. and B.E. Scammell, *Principles of fracture healing*. Surgery (Oxford), 2006. **24**(6): p. 198-207.
2. Giannoudis, P.V., et al., *Accelerated bone healing and excessive callus formation in patients with femoral fracture and head injury*. Injury, 2006. **37**(3, Supplement 1): p. S18-S24.
3. Molven, O., A. Halse, and B. Grung, *Incomplete healing (scar tissue) after periapical surgery--radiographic findings 8 to 12 years after treatment*. Journal of Endodontics, 1996. **22**(5): p. 264-268.
4. Giannoudis, P.V., T.A. Einhorn, and D. Marsh, *Fracture healing: The diamond concept*. Injury, 2007. **38**(Supplement 4): p. S3-S6.
5. Rozen, N., et al., *Transplanted blood-derived endothelial progenitor cells (EPC) enhance bridging of sheep tibia critical size defects*. Bone, 2009. **45**(5): p. 918-924.
6. Marsh, J.L., *Principles of bone grafting: non-union, delayed union*. Surgery (Oxford), 2006. **24**(6): p. 207-210.
7. Sen, M.K. and T. Miclau, *Autologous iliac crest bone graft: Should it still be the gold standard for treating nonunions?* Injury, 2007. **38**(1, Supplement 1): p. S75-S80.
8. Malak, S.F.F. and I.A. Anderson, *Orthogonal cutting of cancellous bone with application to the harvesting of bone autograft*. Medical Engineering & Physics, 2008. **30**(6): p. 717-724.
9. Kessler, P., et al., *Harvesting of bone from the iliac crest--comparison of the anterior and posterior sites*. British Journal of Oral and Maxillofacial Surgery, 2005. **43**(1): p. 51-56.
10. Lewandrowski, K.-U., et al., *Bioresorbable bone graft substitutes of different osteoconductivities: a histologic evaluation of osteointegration of poly(propylene glycol-co-fumaric acid)-based cement implants in rats*. Biomaterials, 2000. **21**(8): p. 757-764.
11. Kim, D.H., et al., *Prospective study of iliac crest bone graft harvest site pain and morbidity*. The Spine Journal, 2009. **9**(11): p. 886-892.
12. Schaaf, H., et al., *Donor site morbidity after bone harvesting from the anterior iliac crest*. Oral Surgery, Oral Medicine, Oral Pathology, Oral Radiology, and Endodontology, 2010. **109**(1): p. 52-58.
13. Russell, J.L. and J.E. Block, *Surgical harvesting of bone graft from the ilium: point of view*. Medical Hypotheses, 2000. **55**(6): p. 474-479.
14. Spallone, A., *A less-invasive technique for harvesting autologous iliac crest grafts for cervical interbody fusion: Technical note*. Surgical Neurology, 2007. **67**(2): p. 160-162.
15. Kinney, R.C.M.D.P., et al., *Demineralized Bone Matrix for Fracture Healing: Fact or Fiction?* Journal of Orthopaedic Trauma
2010. **24** Supplement 1: p. S52-S55.
16. Swenson, C.L. and S.P. Arnoczky, *Demineralization for Inactivation of Infectious Retrovirus in Systemically Infected Cortical Bone: In Vitro and in Vivo Experimental Studies*. J Bone Joint Surg Am, 2003. **85**(2): p. 323-332.
17. Ilan, D.I. and A.L. Ladd, *Bone graft substitutes*. Operative Techniques in Plastic and Reconstructive Surgery, 2002. **9**(4): p. 151-160.
18. Urist, M.R., *Bone: Formation by Autoinduction*. Science, 1965. **150**(3698): p. 893-899.

19. Lee, K.J.H., J.G. Roper, and J.C. Wang, *Demineralized bone matrix and spinal arthrodesis*. The Spine Journal. **5**(6, Supplement 1): p. S217-S223.
20. Kim, H.J., et al., *Bone tissue engineering with premineralized silk scaffolds*. Bone, 2008. **42**(6): p. 1226-1234.
21. Cancedda, R., et al., *Tissue engineering and cell therapy of cartilage and bone*. Matrix Biology, 2003. **22**(1): p. 81-91.
22. Blom, A., (V) *Which scaffold for which application?* Current Orthopaedics, 2007. **21**(4): p. 280-287.
23. Kasten, P., et al., *The effect of platelet-rich plasma on healing in critical-size long-bone defects*. Biomaterials, 2008. **29**(29): p. 3983-3992.
24. Meinel, L., et al., *Silk based biomaterials to heal critical sized femur defects*. Bone, 2006. **39**(4): p. 922-931.
25. Kang, H.-W., Y. Tabata, and Y. Ikada, *Fabrication of porous gelatin scaffolds for tissue engineering*. Biomaterials, 1999. **20**(14): p. 1339-1344.
26. Karageorgiou, V. and D. Kaplan, *Porosity of 3D biomaterial scaffolds and osteogenesis*. Biomaterials, 2005. **26**(27): p. 5474-5491.
27. Ma, P.X., *Biomimetic materials for tissue engineering*. Advanced Drug Delivery Reviews, 2008. **60**(2): p. 184-198.
28. Liu, C., Z. Xia, and J.T. Czernuszka, *Design and Development of Three-Dimensional Scaffolds for Tissue Engineering*. Chemical Engineering Research and Design, 2007. **85**(7): p. 1051-1064.
29. Hutmacher, D.W., *Scaffolds in tissue engineering bone and cartilage*. Biomaterials, 2000. **21**(24): p. 2529-2543.
30. Farrar, G., *Creation of Ovalbumin Based Scaffolds for Bone Tissue Regeneration*. Master's Thesis, Virginia Polytechnic Institute and State University, 2009.
31. Paliwal, M., D. Gordon Allan, and P. Filip, *Failure analysis of three uncemented titanium-alloy modular total hip stems*. Engineering Failure Analysis. **In Press, Corrected Proof**.
32. Olszta, M.J., et al., *Bone structure and formation: A new perspective*. Materials Science and Engineering: R: Reports, 2007. **58**(3-5): p. 77-116.
33. Dorozhkin, S.V. and M. Epple, *Biological and Medical Significance of Calcium Phosphates*. Angewandte Chemie International Edition, 2002. **41**(17): p. 3130-3146.
34. Kokubo, T., *Surface chemistry of bioactive glass-ceramics*. Journal of Non-Crystalline Solids, 1990. **120**(1-3): p. 138-151.
35. Barrere, F., et al., *Nucleation of biomimetic Ca-P coatings on Ti6Al4V from a SBF×5 solution: influence of magnesium*. Biomaterials, 2002. **23**(10): p. 2211-2220.
36. Jayasuriya, A.C., *Acceleration of biomimetic mineralization to apply in bone regeneration* Biomed. Mater., 2008(3): p. 015003.
37. Malafaya, P.B. and R.L. Reis, *Bilayered chitosan-based scaffolds for osteochondral tissue engineering: Influence of hydroxyapatite on in vitro cytotoxicity and dynamic bioactivity studies in a specific double-chamber bioreactor*. Acta Biomaterialia, 2009. **5**(2): p. 644-660.
38. Li, Z., et al., *Chitosan-alginate hybrid scaffolds for bone tissue engineering*. Biomaterials, 2005. **26**(18): p. 3919-3928.
39. Lee, J.B., et al., *PLGA scaffold incorporated with hydroxyapatite for cartilage regeneration*. Surface and Coatings Technology, 2008. **202**(22-23): p. 5757-5761.

40. Link, D.P., et al., *Mechanical evaluation of implanted calcium phosphate cement incorporated with PLGA microparticles*. *Biomaterials*, 2006. **27**(28): p. 4941-4947.
41. Wang, Y., et al., *Improved mechanical properties of hydroxyapatite/poly([var epsilon]-caprolactone) scaffolds by surface modification of hydroxyapatite*. *Applied Surface Science*. **In Press, Corrected Proof**.
42. Wiria, F.E., et al., *Poly-[epsilon]-caprolactone/hydroxyapatite for tissue engineering scaffold fabrication via selective laser sintering*. *Acta Biomaterialia*, 2007. **3**(1): p. 1-12.
43. Bohner, M. and J. Lemaitre, *Can bioactivity be tested in vitro with SBF solution?* *Biomaterials*, 2009. **30**(12): p. 2175-2179.
44. Kokubo, T. and H. Takadama, *How useful is SBF in predicting in vivo bone bioactivity?* *Biomaterials*, 2006. **27**(15): p. 2907-2915.
45. Woodard, J.R., et al., *The mechanical properties and osteoconductivity of hydroxyapatite bone scaffolds with multi-scale porosity*. *Biomaterials*, 2007. **28**(1): p. 45-54.
46. Kim, S.W., et al., *Ghrelin stimulates proliferation and differentiation and inhibits apoptosis in osteoblastic MC3T3-E1 cells*. *Bone*, 2005. **37**(3): p. 359-369.
47. Isama, K. and T. Tsuchiya, *Enhancing effect of poly(-lactide) on the differentiation of mouse osteoblast-like MC3T3-E1 cells*. *Biomaterials*, 2003. **24**(19): p. 3303-3309.
48. Elgendy, H.M., et al., *Osteoblast-like cell (MC3T3-E1) proliferation on bioerodible polymers: an approach towards the development of a bone-bioerodible polymer composite material*. *Biomaterials*, 1993. **14**(4): p. 263-269.
49. Martínez-Ruvalcaba, A., E. Chornet, and D. Rodrigue, *Viscoelastic properties of dispersed chitosan/xanthan hydrogels*. *Carbohydrate Polymers*, 2007. **67**(4): p. 586-595.
50. Brandl, F., F. Sommer, and A. Goepferich, *Rational design of hydrogels for tissue engineering: Impact of physical factors on cell behavior*. *Biomaterials*, 2007. **28**(2): p. 134-146.
51. Nisbet, A.D., et al., *The Complete Amino-Acid Sequence of Hen Ovalbumin*. *European Journal of Biochemistry*, 1981. **115**(2): p. 335-345.
52. Cowin, S.C., *Bone poroelasticity*. *Journal of Biomechanics*, 1999. **32**(3): p. 217-238.
53. Rauch, F., R. Travers, and F.H. Glorieux, *Intracortical remodeling during human bone development--A histomorphometric study*. *Bone*, 2007. **40**(2): p. 274-280.
54. Cahue, S., et al., *The ratio of type II collagen breakdown to synthesis and its relationship with the progression of knee osteoarthritis*. *Osteoarthritis and Cartilage*, 2007. **15**(7): p. 819-823.
55. Seo, J.-H., et al., *Reduction of allergenicity of irradiated ovalbumin in ovalbumin-allergic mice*. *Radiation Physics and Chemistry*. **76**(11-12): p. 1855-1857.
56. Urisu, A., et al., *Allergenic activity of heated and ovomucoid-depleted egg white*. *Journal of Allergy and Clinical Immunology*, 1997. **100**(2): p. 171-176.
57. Kelso, J.M., *Administration of influenza vaccines to patients with egg allergy*. *Journal of Allergy and Clinical Immunology*, 2010. **125**(4): p. 800-802.
58. Congote, L.F., *Similarities in structure and function of bovine serum erythrotropin and human insulin-like growth factor II: Two fetal erythroid cell stimulating factors*. *Biochemical and Biophysical Research Communications*, 1985. **126**(2): p. 653-659.
59. Muramatsu, T., R. Pinontoan, and J.-i. Okumura, *Biopotency of fetal bovine serum, and insulin and insulin-like growth factors I and II in enhancing whole-body protein synthesis of chicken embryos cultured in vitro*. *Comparative Biochemistry and Physiology Part C: Pharmacology, Toxicology and Endocrinology*, 1995. **111**(2): p. 281-286.

60. Personal Communication.
61. Zimmermann, K.A., et al., *Biomimetic design of a bacterial cellulose/hydroxyapatite nanocomposite for bone healing applications*. Materials Science and Engineering: C. **In Press, Corrected Proof.**

Appendix A: Bisphosphonation of Hydroxyethyl Chitosan (HEC)

A.1 Introduction

Including phosphonates and bisphosphonates on natural polymer substrates is not a procedure unique to OVA. Michael addition of bisphosphonates has also been performed on hydroxyethyl chitosan (HEC). The following research discusses a novel bone graft substitute designed with natural proteins and polysaccharides where their surfaces are precisely modified with bisphosphonate groups to enable *in vitro* mineralization of the scaffolds. Biomineralization of the three-dimensional porous sponges can improve cellular response and also yield the high compressive strengths required for bone scaffold applications.

A.2 Materials and Methods

A 2% w/v bisphosphonated HEC solution was created. Scaffolds were made from this solution in a similar manner to the procedure outlined in section 2.1.3. HEC solution was mixed with an amount of either 258 g/mol or 700 g/mol polyethylene glycol (PEG) to reach an amine to acrylate ratio of 0.25. Then, 2.5 mL solution was added to each well of a 12-well plate along with 1 g 150-212 μm NaCl porogen. The plate was placed on a shaker at 50 rpm and 37 °C for 18 hr. The resulting hydrogel was then washed in DI water for 24 hr, frozen overnight and freeze-dried.

Scaffolds were mineralized in 5x SBF for 72 hr with SBF exchanged every 24 hr. A live/dead stain was performed parallel with an MTT assay to measure cytotoxicity.

A.3 Results and Discussion

Bisphosphonates were added to HEC by Michael addition of amine groups on the polymer backbone (Figure 23). Of a targeted 25% conversion of amines, 83% conversion was achieved within 24 hours at room temperature.

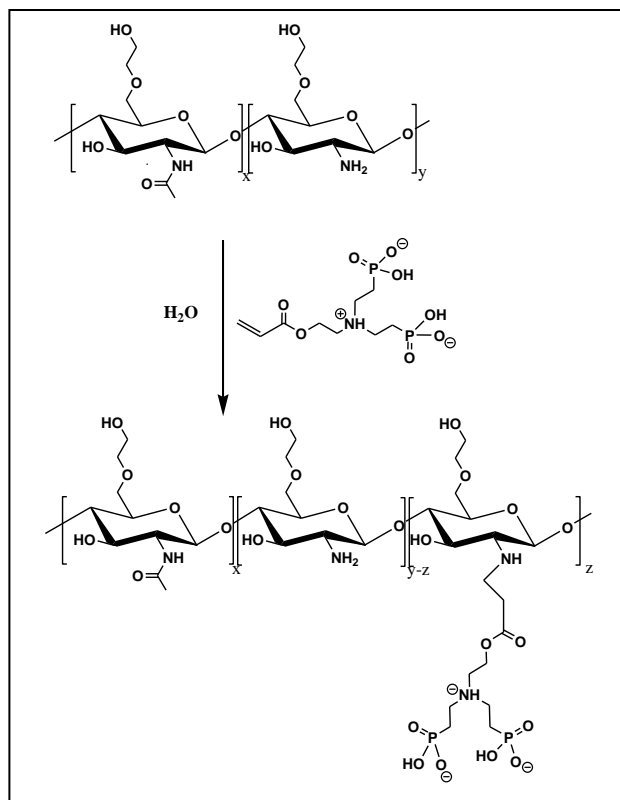


Figure 23: Modification of amine-containing HEC with bisphosphonates via an aza-Michael reaction [60]

PEG of both molecular weights crosslinked the HEC, forming hydrogels. Three-dimensional porous foams were created upon freeze-drying. Optical microscopy showed that both substrates demonstrated a similar structure of interconnecting porosity approximately 200 μm in diameter (Figure 24).

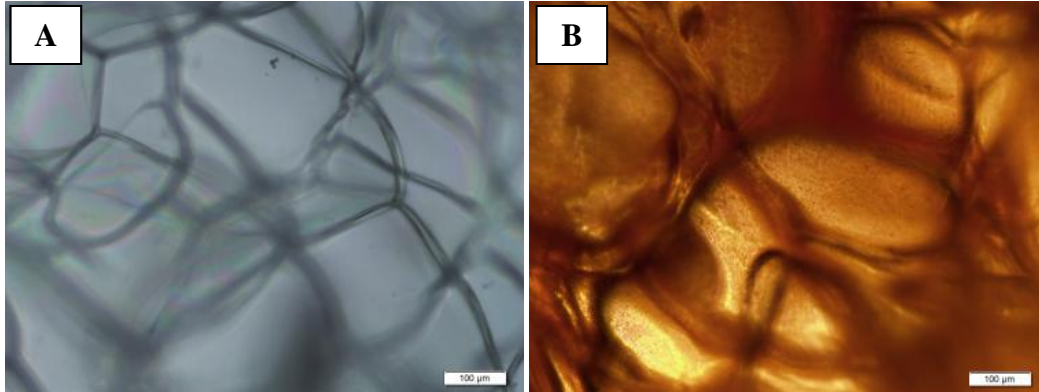


Figure 24: Optical microscopy of HEC (A) and OVA (B) sponges at 100x

HEC scaffolds fully dissolved the NaCl porogen prior to crosslinking. Pores were most likely created during the freezing and freeze-drying phase where ice crystals expanded and sublimed, leaving behind pores of comparable size to those seen in OVA scaffolds.

Cell studies showed that neither mineralized nor unmineralized samples induced a cytotoxic response. MTT assay showed cell viability to be comparable to a control triplicate (Figure). This study has shown that it is possible to introduce bisphosphonates to HEC, crosslink the scaffolds, and mineralize them with 5x SBF without causing cell death.

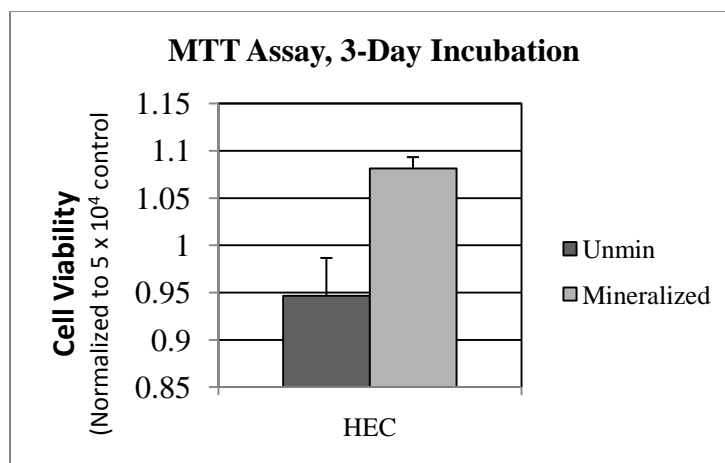


Figure 25: MTT Assay on HEC scaffolds

Appendix B: Biomineralization of Bacterial Cellulose

B.1 Introduction

Biomineralization of natural polymer scaffolds is not limited to OVA and p-OVA substrates. Similar work has been conducted on bacterial cellulose (BC), a fibrous collagen-like polymer spun by the bacteria *Acetobacter xylinum*. The growth of BC substrates was controlled to produce pellicle and tube morphologies as opposed to three-dimensional porous scaffolds as seen with OVA. While each substrate produced mineralization, the inside of the tube surfaces produced the most mineralization. All substrates produced the most minerals under dynamic treatments.

B.2 Materials and Methods

Two BC morphologies were grown, resulting in three substrates: pellicle, tube in, and tube out. The tubes were grown around a cylinder from the inside out, meaning the inside surface was denser than the outside surface. Each of these substrates was charged with carboxymethyl cellulose (CMC) and immersed in 1x SBF at 37 °C for one week. SBF was changed in three ways: unchanged (static), every 24 hr (dynamic), and constantly changed through the use of a bioreactor pump system (continuous). For static treatments, 10ml of SBF were dispensed into six-well plates containing 0.5” by 0.5” charged BC samples and left to mineralize for one week. SBF was changed every 24 hours for the dynamic treatment. A bioreactor was created to provide continuous SBF flow to the tube-shaped BC substrates. The system consisted of an SBF container, a peristaltic pump, and a sample chamber resting in a 37 °C oven. PVC tubing was used throughout.

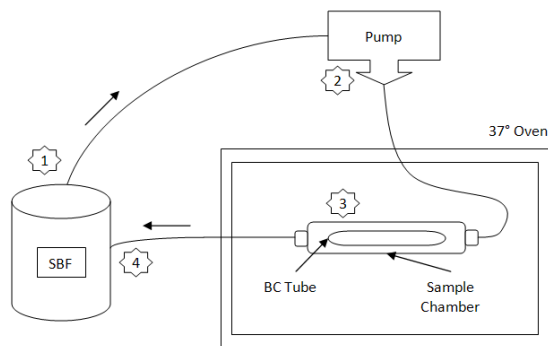


Figure 26: Schematic of a bioreactor/pump system for creation of mineralized BC tubes [61].

Material characterization by XPS was performed using PHI Quantera SXM. FESEM images were taken on freeze-dried samples of both unmineralized and mineralized BC substrates. Built-in EDS was also used to confirm elemental composition. A Phillips Xpert Pro X-Ray Diffraction System was used to conduct XRD. MC3T3-E1 cell studies were performed to determine cytotoxicity and gene expression.

B.3 Results and Discussion

Each SBF treatment yielded Ca-P crystallization on BC substrates. However, as seen in Table 10 below, the highest atomic percentages of Ca and P were seen with dynamic SBF treatments. Statically-treated samples had the next most mineralization, and samples loaded in the bioreactor produced the least amount.

Table 10: Average XPS data for each treatment and substrate [61]

Treatment	Substrate (N*)	At % Ca	At % P	Ca/P Ratio
<i>Static</i>	Pellicle (6)	2.22	1.52	1.50
	Tube In (3)	2.35	1.93	1.26
	Tube Out (3)	1.46	0.98	1.92
<i>Dynamic</i>	Pellicle (5)	7.71	11.18	1.44
	Tube In (2)	5.44	7.97	1.47
	Tube Out (2)	5.00	7.25	1.44
<i>Continuous[†]</i> <i>(Bioreactor)</i>	Tube In (1)	0.60	0.49	1.22
	Tube Out (1)	0.44	0.27	1.63

N* Number of samples tested

[†] The bioreactor sample chamber was constructed with the intent of loading tubes; therefore, no pellicles were tested with this treatment type, so there was no XPS data available for them.

Since all other experimental conditions remained constant, it was determined that the temporal aspect of mineralization played a major role in the amount of mineralization seen. Statically treated samples were given the greatest amount of time to interact with SBF ions; the 10 mL of SBF was left unchanged for one week. These samples mineralized, but reached a mass-limited phase where all available calcium and phosphorus ions had interacted with the BC surfaces prior to the conclusion of the one-week incubation time period. At the other extreme, BC samples mineralized in the bioreactor experienced a continuous flow of ions, resulting in a narrow time window for precipitation onto the scaffold surfaces. Dynamically-treated samples, which were given adequate time for ion-scaffold interaction and refreshed once available ions had precipitated, grew the greatest amount of Ca-P crystals. Figure 27 below shows FESEM images of crystallization on the three dynamically-treated BC substrates.

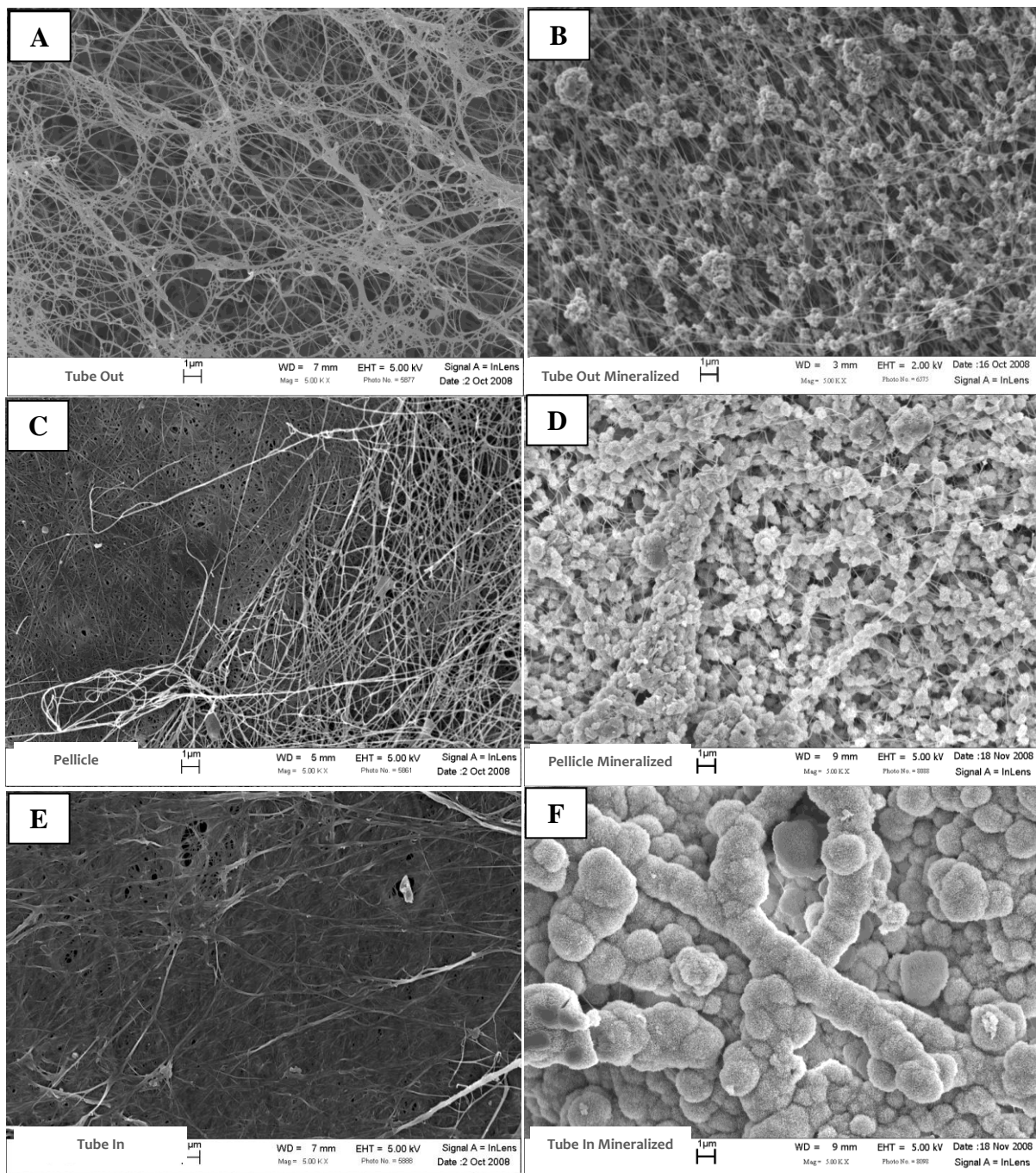


Figure 27: FESEM images taken at the same magnification: (A) pure tube out BC scaffold, (B) mineralized tube out BC scaffold, (C) pure pellicle BC scaffold, (D) mineralized pellicle BC scaffold, (E) pure tube in BC scaffold, (F) mineralized tube in BC scaffold [61].

EDS and XRD were used to determine the phase of Ca-P present on the BC scaffolds. The concentrations of atoms present on and off a Ca-P crystal are compared in Table 11. The spectrum taken on the crystal shows over 22 % Ca and 12 % P, and neither element is present off the crystal.

Table 11: EDS spectrum data of elements present on crystal observed and off of the crystal observed [61].

Element	Spectrum 1 - On crystal		Spectrum 2 - Off crystal	
	Weight %	Atomic %	Weight %	Atomic %
<i>Carbon</i>	22.62	35.78	41.85	55.53
<i>Oxygen</i>	35.06	41.63	30.62	30.50
<i>Sodium</i>	1.21	1.00	6.48	4.49
<i>Chlorine</i>	6.13	3.28	21.05	9.47
<i>Phosphorus</i>	12.36	7.58	0.00	0.00
<i>Calcium</i>	22.63	10.73	0.00	0.00

While identification of Ca-P crystallization is important, many Ca-P crystals can form. XRD was used to determine precisely what crystal phase was present on the BC substrates. Figure 28 shows XRD spectra of pure BC and mineralized BC.

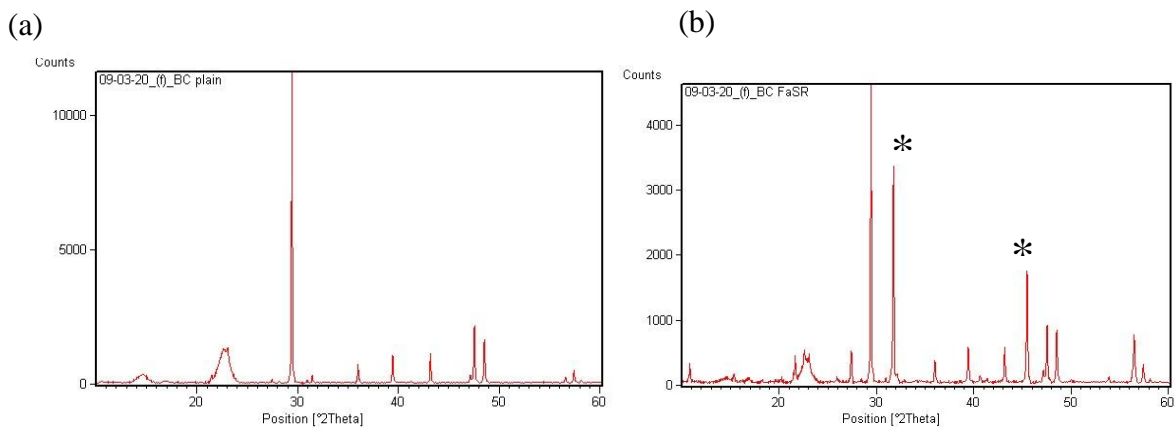


Figure 28: XRD spectra of (a) pure BC and (b) mineralized BC with the asterisks indicating the primary peaks used to identify the calcium phosphate crystal [61].

Two peaks are identified in the mineralized spectra that do not appear in the pure BC spectra. Based on powder diffraction files, these peaks are signatures of calcium-deficient hydroxyapatite (cdHAp).

Cell studies confirm that osteoblast adhesion was preferential to the mineralized samples. In Figure 29, fluorescent microscopy on (A) a pure BC scaffold and (B) a mineralized BC scaffold shows increased confluency on the mineralized scaffold.

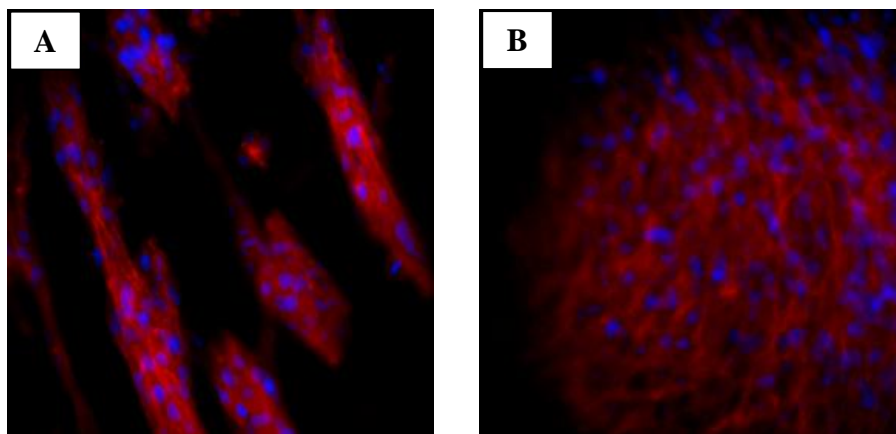


Figure 29: Fluorescent microscopy images (blue stain = nucleus, red stain = actin): (A) pure BC control scaffold and (B) mineralized BC scaffold [61].

ALP activity for MC3T3-E1 preosteoblasts was measured over a 12-day period to measure gene expression. As seen in the image below, ALP levels increased for all substrates compared to the control, but with confidence at 95%, differences were not statistically significant.

Alkaline Phosphatase Activity after 12 Days

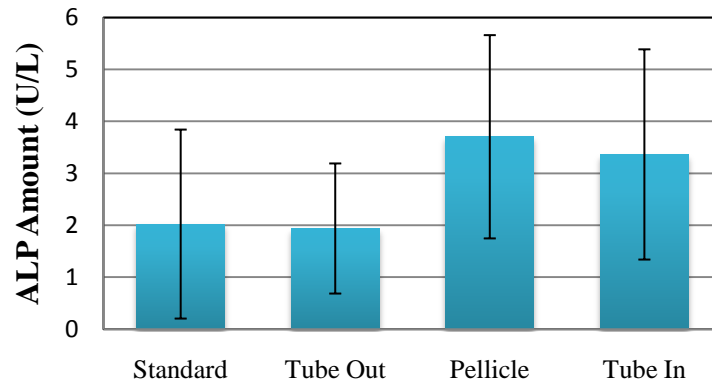


Figure 30: ALP activity for BC substrates [61]

In this study, BC substrates were mineralized with HAp crystals, and cell studies showed that osteoblasts preferred these crystallized substrates to pure BC. Mineralization was best achieved dynamically when ions in SBF were given adequate time to interact with scaffolds.